



Cold spray deposition of lunar regolith on polymeric substrates: A pathway toward in-situ resource utilization on the Moon

Sazedur Rahman ^a, Semih Akin ^{a,b}*

^a Department of Mechanical, Aerospace, and Nuclear Engineering, Rensselaer Polytechnic Institute, Troy, NY 12180, USA

^b Center for Smart Convergent Manufacturing Systems (CSCCMS), Rensselaer Polytechnic Institute, Troy, NY 12180, USA

ARTICLE INFO

Keywords:

Additive manufacturing
Cold spray
Space manufacturing
In-Situ Resource Utilization (ISRU)
Lunar regolith
LHS-1D
Polytetrafluoroethylene (PTFE)

ABSTRACT

In-Situ Resource Utilization (ISRU) plays a crucial role in reducing the cost of lunar exploration and minimizing reliance on Earth-supplied material, both are essential for sustainable human activities on the Moon. In this context, lunar regolith serves as a key source for ISRU in lunar exploration, supporting applications such as manufacturing, construction, shielding, and so on. In particular, the development of functional coatings from regolith is crucial for enhancing component performance and enabling sustainable in-situ repair in space environments. While efforts have been done to investigate lunar regolith deposition on metals, studies on polymeric substrates remains largely limited, thereby highlighting the need for innovative approaches in this domain. This study explores the use of Cold Spray Additive Manufacturing (CSAM) to deposit lunar regolith simulant onto polymeric substrates, with the aim of developing functional coatings that can advance future ISRU efforts on the Moon. In this regard, CSAM of regolith simulant (LHS-1D) on polytetrafluoroethylene (PTFE) substrate is studied, as PTFE is widely used in space applications for its desired properties (e.g., chemical resistance, thermal stability, low-friction). A comprehensive design of experiments was implemented to investigate the process–structure–property relationships of CSAM and to identify optimal process settings. The resulting coatings are characterized in terms of microstructure, mechanical properties, hardness, adhesion strength, and thermal resistance to holistically assess their performance. The as-CSAM specimens developed regolith coatings (12–23 µm) with excellent adhesion (5B per ASTM D3359 and ~ 9–12 MPa from pull-off tests), while largely preserving their mechanical properties. In addition, the fabricated regolith coatings improved the thermal resistance (~ 8.25%) compared with pristine PTFE. This work represents the first attempt to evaluate the feasibility of CSAM for producing coatings from lunar regolith on polymeric substrates, with the goal of supporting space manufacturing and long-term lunar missions.

1. Introduction

The exploration of the Moon as our closest celestial neighbor has fascinated humanity for centuries. Since the first Apollo missions in the late 1960s, lunar exploration has regained priority for both space agencies and private enterprises [1]. In this context, Artemis mission [2] and numerous robotic and manufacturing endeavors [3] highlight a commitment to establishing a sustainable presence on the lunar surface. However, long-term lunar operations present significant challenges, particularly in terms of constructing habitats, infrastructure, and other mission-critical systems. A major obstacle is the logistical and economic impracticality of transporting large quantities of materials from Earth to the Moon [4]. For instance, sending one kilogram of payload to the Moon costs approximately \$1 million using NASA's Space Launch System (SLS) for the Artemis mission [5], and about \$1.2 million using

United Launch Alliance (ULA)'s Vulcan Centaur rocket [6]. While commercial launch providers such as SpaceX are expected to substantially reduce launch costs, the overall cost of delivering payloads to the Moon remains considerable (i.e., approximately \$100,000/kg for SpaceX's Starship) [7].

To address this challenge, In-Situ Resource Utilization (ISRU) [8] has emerged as a transformative approach. ISRU focuses on using lunar regolith, which is the fine dust and rock covering the Moon's surface, to support construction, maintenance, and manufacturing needs [9,10]. Regolith is abundant and readily available, consisting primarily of oxides, including SiO_2 (~49.16 wt%), Al_2O_3 (~26.29 wt%), CaO (~13.52 wt%), FeO (~3.2 wt%), and other minor oxides (i.e., MnO , MgO , Na_2O , P_2O_5 , LOI) [11,12]. This composition makes it a sustainable natural resource that can reduce dependence on Earth-based supplies and significantly lower mission costs. To effectively utilize lunar regolith, researchers

* Corresponding author at: Department of Mechanical, Aerospace, and Nuclear Engineering, Rensselaer Polytechnic Institute, Troy, NY 12180, USA.
E-mail address: akins@rpi.edu (S. Akin).

Nomenclature

Symbols

E	Elastic modulus	NS	Nozzle speed
P	Pressure	R	Universal gas constant
S_a	Surface roughness	t	Coating thickness
T	Temperature	V	Volume
Greek letters			
ρ	Density	ν	Poisson's ratio
Abbreviations			
Adj MS	Adjusted mean square	EDX	Energy-dispersive X-ray spectroscopy
Adj SS	Adjusted sum of squares	ISRU	In-situ resource utilization
AM	Additive manufacturing	LHS	Lunar highlands simulant
ANOVA	Analysis of variance	PEEK	Polyetheretherketone
CS	Cold spray	PI	Polyimide
CSAM	Cold spray additive manufacturing	PTFE	Polytetrafluoroethylene
DF	Degrees of freedom	SEM	Scanning electron microscopy
DoE	Design of experiments		

are increasingly leveraging additive manufacturing (AM) technologies for their ability to produce on-demand production [13–15]. Techniques such as laser powder bed fusion [16–20], laser-directed energy deposition [21–23], material extrusion [24–28], vat polymerization [29–31], and aerosol jet printing [32] have been explored to convert regolith into functional components. Although inherent lunar environmental factors (i.e., microgravity, vacuum, radiation) are often not considered in many of these studies due to experimental challenges and costs, this body of work has advanced our understanding, demonstrating the promising potential of AM for ISRU, in terms of rapid prototyping, on-site maintenance, and repair of essential components.

In addition to part-level AM, surface coatings are equally critical in space manufacturing and ISRU to ensure the point-of-need functionality and longevity of space components in the harsh lunar environment. Surface coatings can enhance the durability, thermal resistance, and mechanical properties of components exposed to the extreme lunar conditions, providing protection against abrasive regolith dust, high radiation, and temperature fluctuations [33]. However, studies on surface manufacturing for space applications and ISRU remain largely limited. While aerosol deposition [32,34,35] and plasma spray [36] have been reported to achieve functional coatings, these methods have primarily focused on metallic substrates. Moreover, such methods may present challenges when depositing functional materials onto polymeric substrates. For instance, aerosol deposition may be ineffective on intrinsically hydrophobic polymers such as PTFE, while plasma spraying can deteriorate polymeric substrates due to the high thermal loads involved. On the one hand, polymeric substrates (e.g., PTFE, PEEK, PI) are critically important in space applications due to their thermal stability, chemical resistance, light-weight, mechanical strength, and low out-gassing. [37]. Although efforts have been made to investigate the wear performance of lunar regolith on PTFE and PEEK substrates for sealing applications [38,39], these studies primarily utilized bulk regolith powder rather than surface-deposited coatings. As such, there remains a significant gap in the literature concerning the exploration of lunar regolith surface deposition on polymeric substrates to advance in-space manufacturing and ISRU.

To contribute to this emerging field, this study evaluates the feasibility of the Cold Spray Additive Manufacturing (CSAM) technique to achieve lunar regolith simulant coatings on polymeric substrates under terrestrial conditions. We hypothesize that CSAM, due to its unique features (viz., solid-state processing, low-temperature deposition, the ability to form dense coatings, sustainable repairing capabilities [40]) may facilitate the high-strength deposition of lunar regolith on polymeric substrates. Although prior studies have explored the cold spraying of various functional materials (e.g., metals, ceramics) on

polymeric substrates, [41,42] to the best of our knowledge, no existing work has investigated the cold spray deposition of lunar regolith simulant on polymeric substrates. In this regard, polytetrafluoroethylene (PTFE), also known as Teflon, was chosen as the substrate due to its widespread use in space applications [38,43]. CSAM, owing to its solid-state processing capability, can enable the deposition of lunar regolith onto intrinsically hydrophobic materials such as PTFE [44], which is challenging for solvent-based methods like aerosol printing and inkjet printing.

In this study, a full factorial design of experiments (DoE) is developed to investigate the effects of key CSAM parameters (e.g., gas pressure, temperature, nozzle traverse speed) on the deposition process, aiming to uncover the underlying process–structure–property relationships. The resulting regolith coatings are thoroughly characterized in terms of microstructure, morphology, chemical composition, mechanical performance, hardness, adhesion strength, and thermal resistance. This work pioneers the use of CSAM for lunar regolith deposition on polymeric substrates, providing critical insights into its feasibility under terrestrial conditions while contributing to the advancement of in-space manufacturing and ISRU applications. Further research will be essential to address the challenges of the lunar environment, including microgravity, vacuum, and radiation.

2. Materials and methods

2.1. Materials

Lunar highlands simulant (LHS-1D) [12,45] – a powder-form lunar regolith simulant – was procured (*Space Resource Technologies, USA*) as the feedstock material for the CSAM process. LHS-1D is specifically designed to replicate the composition and properties of lunar highlands soil, characterized by its heavily cratered regions [12]. It captures the mineralogical makeup and rock fragment composition of the actual lunar highlands [12]. The morphology and particle size distribution of the lunar simulant regolith are shown in Fig. 1a, along with its bulk chemistry in Fig. 1b [12]. Given the fine particle size distribution of the powders (i.e., 0.04–35 μm , with a mean diameter of $\approx 10 \mu\text{m}$) (see Fig. 1a), they were dried at 200 °C for 72 h to remove moisture content and enhance powder flowability for the CSAM process. Note that the terms “lunar regolith simulant” and “lunar regolith” are used interchangeably throughout this work.

As for the substrate, polytetrafluoroethylene (PTFE, *McMaster*) was chosen due to its widespread application in space-related fields, such as thermal insulation, sealing components, and wiring insulation [46,

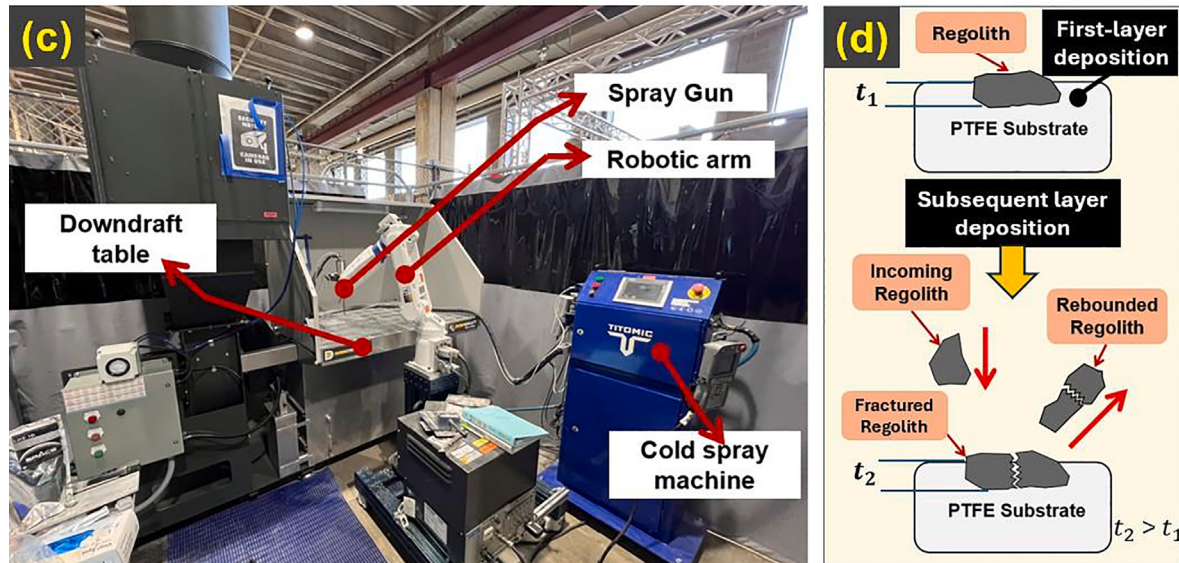
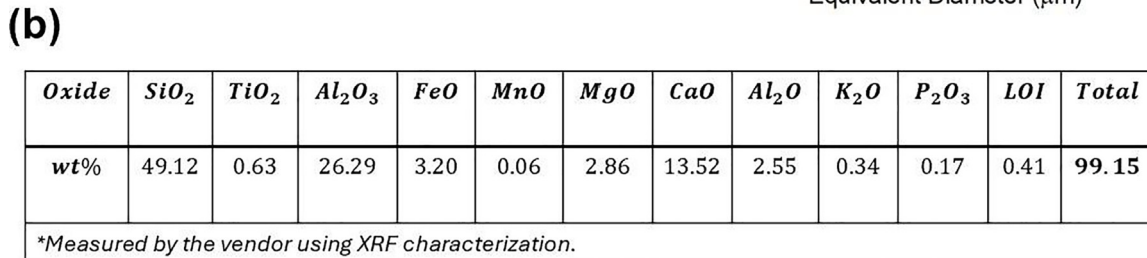
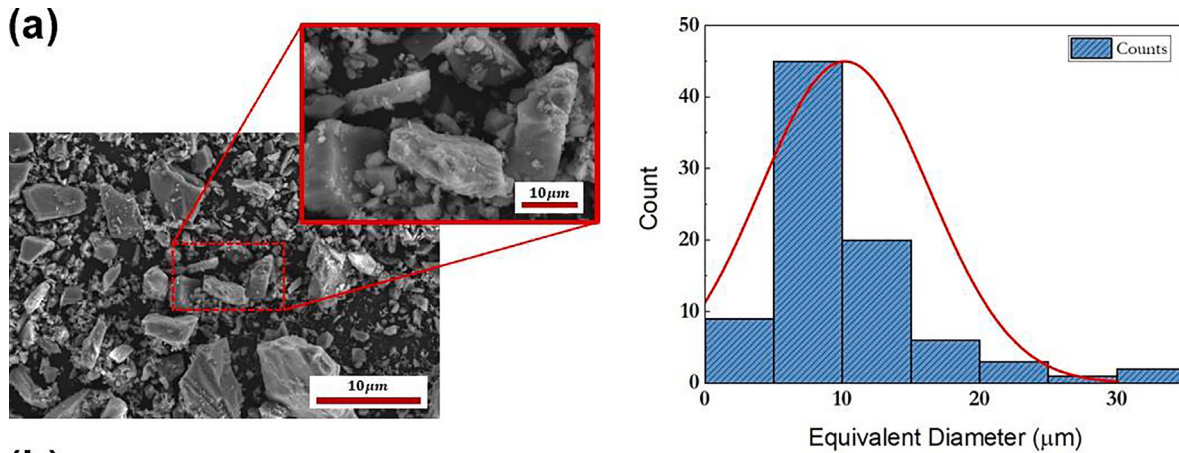


Fig. 1. (a) Morphology of LHS-1D lunar regolith simulant powders (left panel) and corresponding size distribution (right panel); (b) Bulk chemical composition of the LHS-1D powders provided by the vendor; (c) the CSAM experimental setup; (d) illustration of CSAM of regolith powders on polymeric substrates.

[47], owing to its chemical resistance, thermal stability, and low friction properties. Although other high-performance polymers—such as polyimide (Kapton film) and polyether ether ketone (PEEK)—are also widely employed in space systems due to their excellent mechanical and thermal properties [37], these materials pose significant challenges during CSAM. Specifically, polyimide thermoset cannot plastically deform or soften under heat [48], while PEEK's high stiffness and surface hardness may impede effective particle anchoring [49]. In contrast, PTFE's relatively low hardness and compliant surface make it a more favorable candidate for exploring regolith deposition via CSAM. It is noteworthy that future studies may extend this work to other space-qualified polymers (e.g., PEEK) by employing surface modification strategies to enhance their cold-spray processability.

2.2. Cold spray additive manufacturing (CSAM)

CSAM is a solid-state additive manufacturing technique, in which micron-scale particles (5–100 μm) are accelerated through a supersonic nozzle and deposited onto a substrate upon impact to form a coating [50]. Unlike traditional thermal spray methods, CSAM avoids melting the feedstock material, thereby minimizing undesirable phase transformations, residual stresses, and oxidation [51]. This makes it particularly attractive for applications where material properties must be preserved, and for materials sensitive to high temperatures, such as polymeric substrates.

In this study, a low-pressure cold spray system (Titomic D-523) was used, with the deposition nozzle mounted on a multi-axis robotic arm

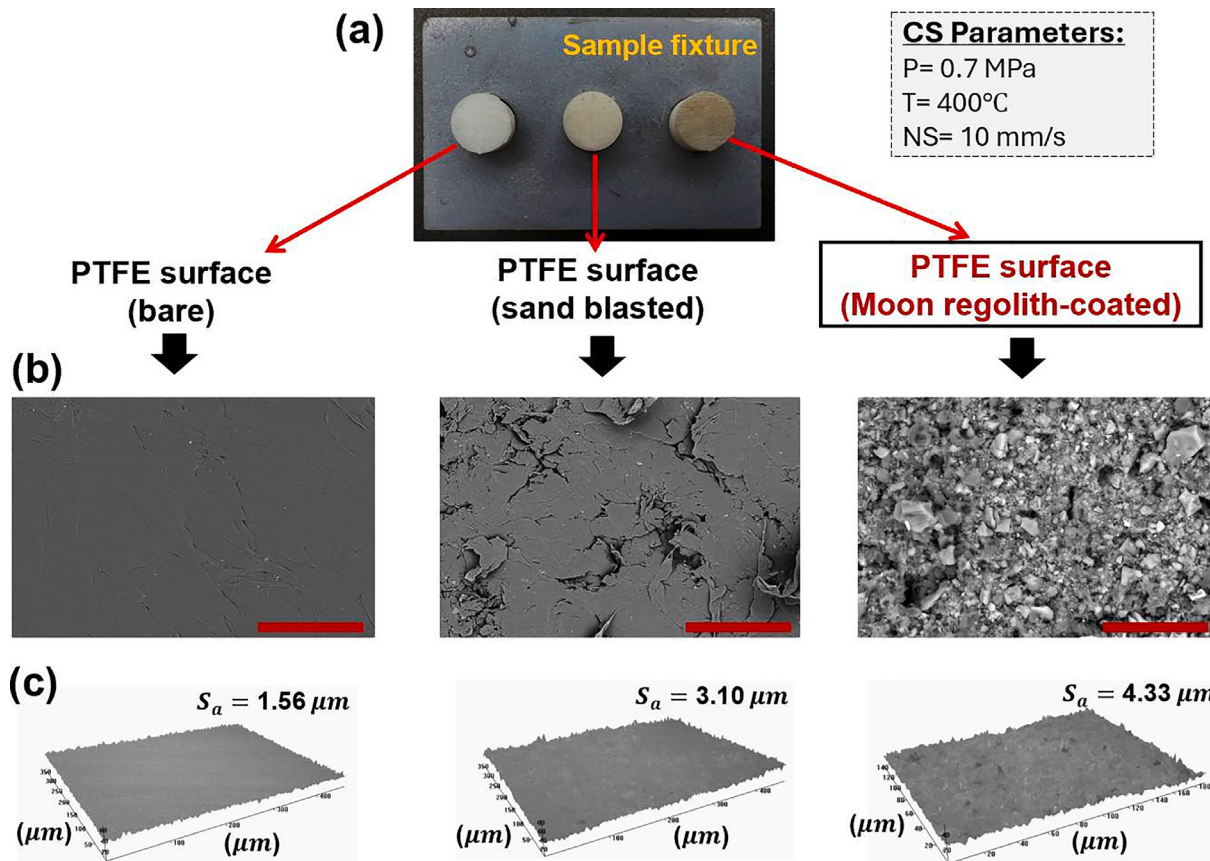


Fig. 2. (a) PTFE samples mounted in the fixture; (b) Microstructure of PTFE surface; bare (left), sand-blasted (middle), and as-CSAM (right); (c) corresponding surface topologies, (SEM scale = 30 μm).

(Yaskawa), as shown in Fig. 1c. This setup ensures precise control of deposition parameters and consistent coating quality, making it well-suited for regolith coatings under controlled conditions. Notably, low-pressure cold spray systems may offer distinct advantages over high-pressure cold spray systems due to their compact design and lower operational requirements, which enable mobile and handheld operation [52]. Such portability could facilitate point-of-need, on-site repair, coating, and maintenance tasks on the lunar surface by astronauts, where flexibility, ease of handling, and low power consumption are critical for in-situ mission sustainability.

Prior to cold spray (CS) deposition of regolith powders, the PTFE surface was activated by sandblasting with 400-grit sands. This process generates micro-rough anchoring points, facilitating the embedding of regolith particles into the polymer matrix (see Fig. 1d). Fig. 2 compares the CS regolith deposition on PTFE specimens under various surface conditions. In detail, Fig. 2a presents the bare PTFE surface before (left) and after (middle) sandblasting, highlighting the increase in surface roughness, which is evident in the corresponding SEM and optical profilometer images shown in Fig. 2b–c, respectively. Fig. 2c exhibits that the surface roughness value (S_a) increased from 1.56 μm to 3.10 μm after sandblasting. In addition, the right-hand sample in the fixture in Fig. 2a represents the PTFE surface following CS regolith deposition, with the corresponding SEM image in Fig. 2b confirming successful regolith deposition. Meanwhile, Fig. 2c depicts the optical profilometer image, revealing an increase in surface roughness (S_a), with a value of 4.33 μm . A full factorial design of experiment (DoE) is generated using Minitab software to analyze the CS deposition of lunar regolith on the PTFE surface, as detailed in Section 3.1.

2.3. Characterization

The microstructure of the regolith deposited specimens were analyzed by using both optical microscopy (Olympus GX53) and scanning electron microscopy (SEM, FEI Versa). In addition, Energy Dispersive X-ray Spectroscopy (EDX) was employed to determine the chemical composition of the coatings. For cross-sectional microstructure evaluation, specimens were cold-mounted in resin mixture (90% resin and 10% hardener). After 24 h of curing, the mounts were sequentially polished with abrasive papers (grit 240, 400, 600, 1200), followed by micron-scale polishing with 15 μm abrasive media to obtain a smooth, polished surface suitable for SEM and EDX. To minimize charging on the PTFE substrate, all specimens were sputter-coated with a thin layer of platinum (Pt) prior to microscopic analysis. Coating thickness was determined from SEM images using ImageJ software, and areal surface roughness (S_a) of the coatings was measured with an optical profilometer (Zeta-20).

Mechanical tests (tensile tests) were conducted using a universal tensile test machine (Instron 4204) to evaluate the mechanical performance of the coated specimens and quantitatively assess coating-induced changes in strength and ductility. The hardness of the coatings was evaluated via nano-indentation (Hysitron TI900) using a Berkovich indenter, with load-displacement data analyzed by the Oliver-Pharr method. The adhesion strength of the resulting coatings was evaluated using both qualitative methods, (i.e., cross-cut tests following ASTM D3359 [53]), and quantitative methods (i.e., the pull-off adhesion test in accordance with ASTM D4541 [54]). An adhesion tester (Elcometer 510) was employed to measure the interfacial adhesion strength between the polymer substrate and the regolith coatings.

Table 1

Factors, levels, and responses in the design of experiments (DOE).

Factors	Levels			Response
Pressure (MPa)	0.5	0.6	0.7	Coating thickness (μm)
Temperature (°C)	300	400	—	Surface roughness (μm)
Nozzle speed (mm/s)	10	25	50	—

To evaluate the functionality of the regolith coating, a thermal resistance case study was conducted using a programmable heat gun (*SEEKONE*) positioned above a regolith-coated PTFE specimen. A thin-film Type-J thermocouple (*OMEGA*, operating range = -17 °C to 260 °C) was affixed to the center of the specimen's bottom surface, and continuous temperature measurements were recorded through a data acquisition unit (*DATAQ DI-2008 Instruments*). Detailed procedures for each characterization are provided in their respective sections. For all characterization studies, a minimum of three specimens were used to ensure statistical validity and reproducibility of the results.

3. Results and discussion

In this section, first, a DoE was constructed to identify the key process parameters influencing CSAM performance. Next, an optimization study of the CSAM process was conducted to achieve maximum regolith coating thickness with minimal surface roughness. Subsequently, comprehensive characterization studies (i.e., microstructure, mechanical properties, hardness, adhesion, thermal) were conducted to gain insights into the quality and functionality of the fabricated regolith coatings.

3.1. Design of experiments (DoE)

A full-factorial DoE was developed to investigate the individual and interactive effects of CSAM process parameters on the regolith, as it is a well-established approach in CS literature [55]. In this regard, gas pressure (MPa), gas temperature (°C), and nozzle speed (mm/s) were selected as the primary factors for the DoE. Three pressure levels (0.5, 0.6, and 0.7 MPa), two temperature levels (300 and 400 °C), and three nozzle speed levels (10, 25, and 50 mm/s) were selected, as summarized in **Table 1**. In all coating experiments, the spray distance between the nozzle and the substrate was fixed at 30 mm. The responses measured from the DoE are coating thickness (μm) and areal surface roughness (μm). Given that the functional performance of the regolith coatings primarily depends on coating thickness and surface morphology, the other coating properties (i.e., hardness, adhesion strength) were evaluated only for the optimal CSAM settings that produced the maximum coating thickness while minimizing surface roughness. This approach is intended to identify an optimized baseline for CSAM, which is used for subsequent characterizations (Sections 3.3–3.6). **Table 2** summarizes the full-factorial experimental design with the corresponding response values obtained from each run.

The experimental results from the DoE in **Table 2** were mapped into contour plots to visualize and analyze the effects of CSAM process parameters on the coating thickness and surface roughness of the resulting regolith deposits (see **Fig. 3**). Coating thickness was measured at five different locations of each SEM cross-sectional image. For each CSAM condition, the average coating thickness and corresponding standard deviations was calculated from these measurements (see **Table 2**). As shown in **Fig. 3a–b**, the thickness of the coating increased with rising temperature and pressure. In the CSAM process, elevated gas pressure and temperature result in higher gas velocities due to kinetic energy gain, as described by the ideal gas law ($PV = nRT$). This, in turn, enhances momentum transfer to the particles, leading to higher particle impact velocities [56]. This enhanced velocity promotes deeper penetration of regolith particles into the substrate, resulting

Table 2

Full-factorial DoE and corresponding responses.

Run No.	Pressure (MPa)	Temperature (°C)	Nozzle speed (mm/s)	Coating thickness (μm)	Surface roughness, S_a (μm)
1	0.5	300	10	10.94 ± 2.01	2.96
2	0.5	300	25	9.37 ± 0.67	2.28
3	0.5	300	50	5.68 ± 1.03	2.39
4	0.6	300	10	13.85 ± 1.05	2.99
5	0.6	300	25	9.56 ± 0.94	3.69
6	0.6	300	50	7.04 ± 1.29	5.47
7	0.7	300	10	15.61 ± 2.37	2.94
8	0.7	300	25	10.29 ± 2.65	2.63
9	0.7	300	50	7.68 ± 0.56	4.37
10	0.5	400	10	13.07 ± 2.08	3.48
11	0.5	400	25	9.91 ± 1.28	4.46
12	0.5	400	50	8.51 ± 0.71	2.80
13	0.6	400	10	13.99 ± 1.53	4.61
14	0.6	400	25	9.97 ± 0.28	3.10
15	0.6	400	50	8.56 ± 1.12	3.97
16	0.7	400	10	15.86 ± 1.25	4.33
17	0.7	400	25	11.57 ± 2.81	4.22
18	0.7	400	50	8.63 ± 0.74	3.71

in thicker coating deposition (see **Fig. 4a–d**). Additionally, at elevated temperatures, both particles and the substrate become softer and more ductile [57], allowing particles to impinge more effectively into the substrate. This enhanced impingement improves particle–substrate interlocking, ultimately resulting in the formation of thicker coatings.

A comparison of **Fig. 3a–b** reveals that increasing the gas temperature from 300 °C to 400 °C leads to greater sensitivity of the coating thickness to processing conditions, suggesting that the deposition process becomes more responsive to thermal input. At elevated temperatures, the substrate becomes more compliant, allowing regolith particles to embed more effectively. This enhanced particle–substrate interaction promotes mechanical interlocking, resulting in thicker coating deposition. Similarly, increasing the gas pressure also yielded to thicker regolith deposition, as evident from the SEM images in **Fig. 4a–d**.

Conversely, increasing the nozzle speed resulted in thinner coatings. As shown in **Fig. 3a–b**, the coating thickness decreased with higher nozzle speed, regardless of gas pressure and temperature. This effect can be attributed to the reduced residence time of particles in the deposition zone, which lowers the efficiency of particle–substrate interlocking [58]. Microstructural analysis in **Fig. 4c–f** further confirmed the reduction in coating thickness with increasing nozzle speed.

For surface roughness, **Fig. 3c–d** illustrate its relationships with gas pressure and nozzle speed at constant gas temperatures of 300 °C and 400 °C, respectively. Surface roughness generally tended to increase with gas pressure and temperature, as it leads to increased particle velocity and stronger impacts, promoting fragmentation of regolith particles with the polymer (see **Fig. 1d**). This effect leads to more irregular and non-uniform surface deposition, particularly at elevated gas pressures and temperatures (see **Fig. 3c–d**). A similar trend can be also observed from the as-regolith deposited surface topologies in **Fig. 4b** and d (right panels). On the one hand, increasing the nozzle speed led to rougher surface deposition, particularly at speeds exceeding 25 mm/s. This effect can be attributed to the reduced particle impact overlap. Specifically, at higher nozzle traverse speeds, the time spent depositing particles over a given substrate area decreases, leading to uneven coverage, and consequently increase in surface roughness.

The combined effects of CSAM process parameters (i.e., gas pressure, temperature, nozzle speed) on coating thickness and surface roughness were mapped into the ternary plots as shown in **Fig. 3e** and f, respectively. Notably, these plots can reduce reliance on trial-and-error and serve as valuable tools for identifying process-specific conditions to achieve the desired regolith coating thickness and surface roughness.

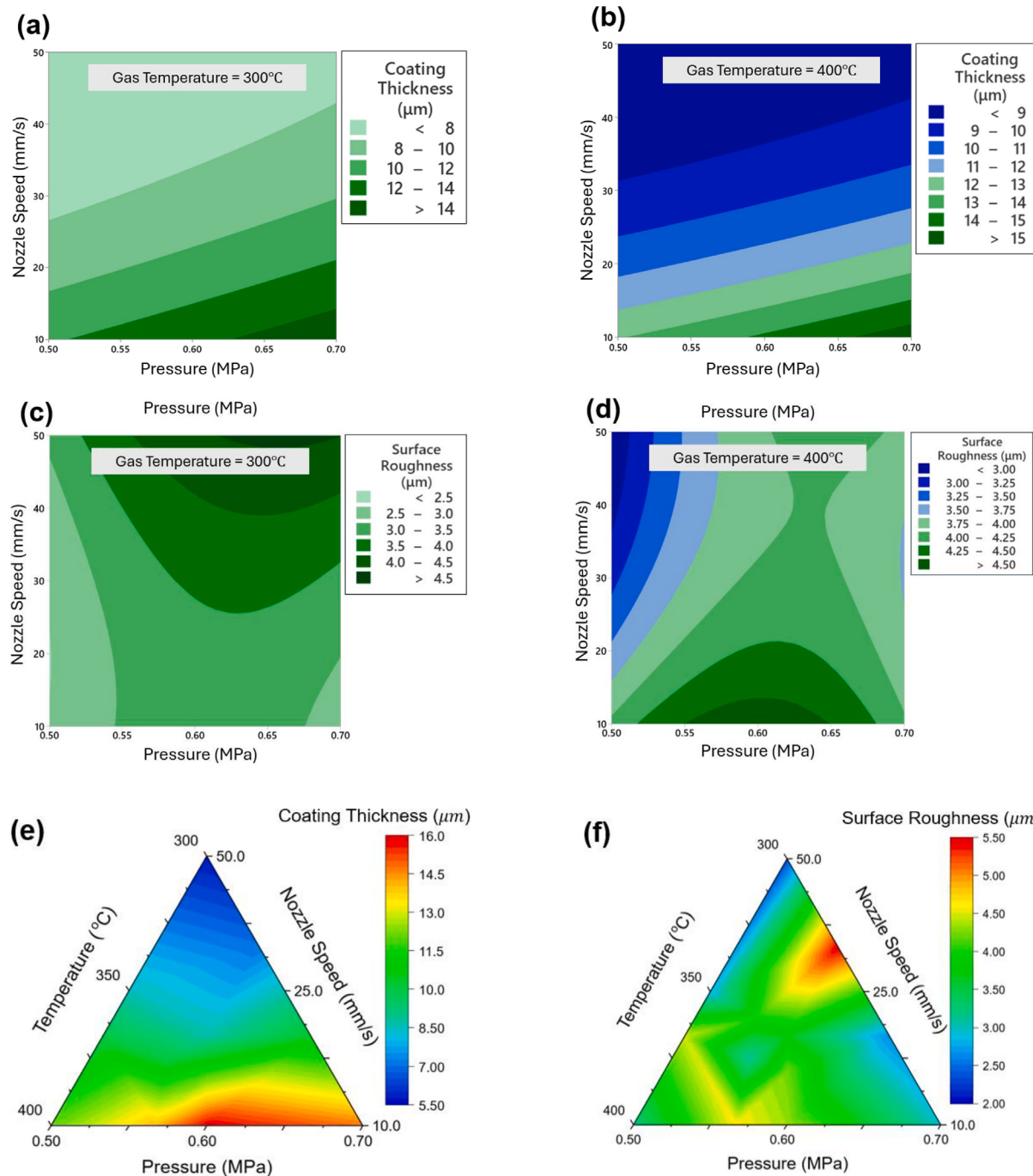


Fig. 3. Surface plots of the resulting coating thickness at (a) $T = 300\text{ }^{\circ}\text{C}$ and (b) $T = 400\text{ }^{\circ}\text{C}$; surface plots of surface roughness at (c) $T = 300\text{ }^{\circ}\text{C}$ and (d) $T = 400\text{ }^{\circ}\text{C}$; Combined influence of CSAM operational parameters on (e) coating thickness and (f) surface roughness.

3.2. Process optimization

Analysis of variance (ANOVA) was conducted to evaluate the statistical influence of CSAM parameters on coating thickness and surface roughness, which are both key factors for the practical implementation of regolith-deposited surfaces in space applications. The ANOVA results for coating thickness in Table 3 indicate that nozzle speed, temperature, and pressure all have a statistically significant effect on the coating thickness ($p < 0.05$), with the gas temperature and nozzle speed being the most influential, followed by temperature and pressure. Among the interaction effects, neither interaction was found statistically significant ($p > 0.05$).

On the other hand, the effects of CSAM parameters on surface roughness were not as pronounced as those on coating thickness, with all results showing $p > 0.05$, as presented in Table 4. This may be attributed to the stochastic nature of particle–substrate interactions in the CSAM process, driven by the two-phase turbulent flow [59]. However, based on the ANOVA results in Table 4, temperature and its interaction with nozzle speed were identified as the principal contributors to variations in surface roughness. Taken together, the ANOVA results in Tables 3 and 4 suggest that optimizing nozzle speed and temperature should be the primary focus followed by gas pressure in order to most effectively control the coating thickness response.

Following the ANOVA analyses, Response Surface Methodology (RSM) [60] was employed to establish empirical relationships between

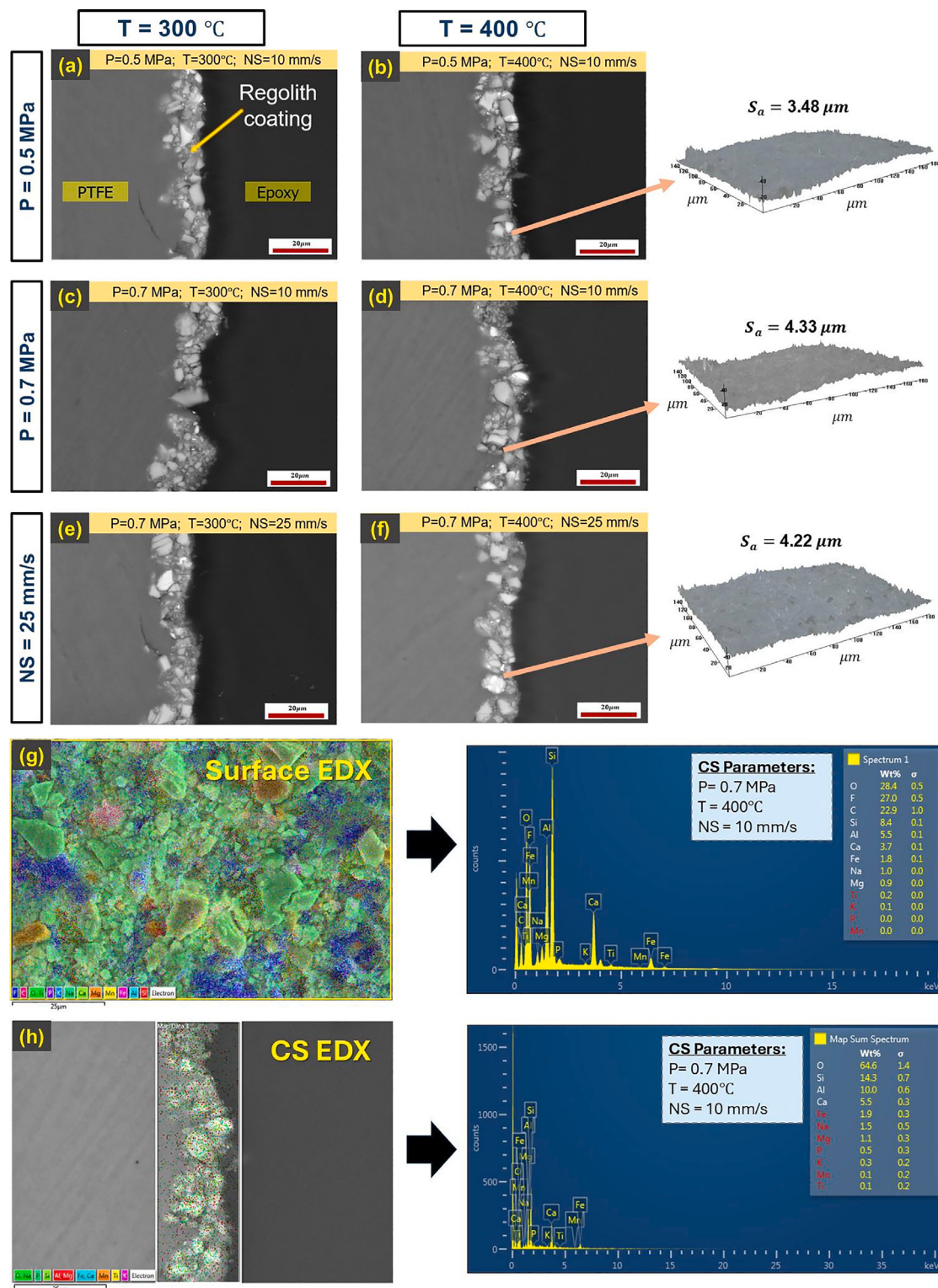


Fig. 4. Microstructure and surface topology of the regolith-deposited PTFE specimens at various CSAM settings: (a) $P = 0.5 \text{ MPa}$, $T = 300^\circ\text{C}$, $NS = 10 \text{ mm/s}$; (b) $P = 0.5 \text{ MPa}$, $T = 400^\circ\text{C}$, $NS = 10 \text{ mm/s}$; (c) $P = 0.7 \text{ MPa}$, $T = 300^\circ\text{C}$, $NS = 10 \text{ mm/s}$; (d) $P = 0.7 \text{ MPa}$, $T = 400^\circ\text{C}$, $NS = 10 \text{ mm/s}$; (e) $P = 0.7 \text{ MPa}$, $T = 300^\circ\text{C}$, $NS = 25 \text{ mm/s}$; (f) $P = 0.7 \text{ MPa}$, $T = 400^\circ\text{C}$, $NS = 25 \text{ mm/s}$; and EDX maps of the (g) surface and (h) cross-section (Scale in SEM images = 20 μm).

Table 3
ANOVA response table for the coating thickness.

Source	DF	Adj SS	Adj MS	F-Value	P-Value
Pressure (MPa)	2	12.379	6.1896	20.14	0.008
Temperature (°C)	1	5.608	5.6080	18.25	0.013
Nozzle speed (mm/s)	2	117.172	58.5861	190.66	0.000
Pressure (MPa) × Temperature (°C)	2	1.167	0.5833	1.90	0.263
Pressure (MPa) × Nozzle speed (mm/s)	4	4.748	1.1869	3.86	0.109
Temperature (°C) × Nozzle speed (mm/s)	2	0.960	0.4801	1.56	0.315
Error	4	1.229	0.3073		
Total	17	143.263			

CSAM process parameters, coating thickness, and surface roughness, while simultaneously optimizing the settings to maximize the thickness and minimizing surface roughness. To this end, a multi-objective optimization model was developed, as presented in Eqs. (1)–(3). The model seeks to identify the optimal CSAM settings (i.e., temperature, pressure, nozzle speed) that achieve these objectives within the design space defined in Eq. (3).

$$\begin{aligned} \text{Maximize: } t(P, T, NS) = & -2.3 + 24.3P + 0.0342T - 0.292NS + 10P^2 \\ & + 0.003863NS^2 - 0.0502PT \\ & - 0.304PNS + 0.000250TNS \end{aligned} \quad (1)$$

$$\begin{aligned} \text{Minimize: } Sa(P, T, NS) = & -25.8 + 74.6P + 0.0265T \\ & + 0.042NS - 59.1P^2 \\ & + 0.00065NS^2 - 0.0132PT \\ & + 0.144PNS - 0.000462TNS \end{aligned} \quad (2)$$

$$\begin{aligned} \text{subject to: } & 0.5 \leq P \leq 0.7 \quad (\text{MPa}) \\ & 300 \leq T \leq 400 \quad (\text{°C}) \\ & 10 \leq NS \leq 50 \quad (\text{mm/s}) \end{aligned} \quad (3)$$

Fig. 5 compares the experimental results (see Table 2) with the predicted values obtained from Eqs. (1)–(2). As shown in Fig. 5a, a strong goodness of fit was achieved between the experimental results and modeling predictions, with an R^2 value of 96.23%. The surface mapping in Fig. 5b further confirms this agreement. On the other hand, R^2 value of 72.46% was obtained for surface roughness (see Fig. 5c–d), which is likely due to the inherent variability in particle impingement and surface morphology during the CSAM process.

After the fitting tests, the global maximum value of coating thickness and the global minimum value of surface roughness within the design space are identified as shown in Fig. 6. The optimal CSAM settings that maximize the coating thickness and minimize the surface roughness were achieved as $P = 0.7$ MPa, $T = 300$ °C and $NS = 10$ mm/s, which led to a coating thickness of ~ 15.41 μm and surface roughness of ~ 2.78 μm, as illustrated in Fig. 6. The Energy Dispersive X-ray Spectroscopy (EDX) analysis of the regolith-coated sample under optimal process conditions, shown in Fig. 4g–h, confirmed the distribution of key elemental constituents across the surface and cross-section, indicating successful deposition of regolith onto the PTFE substrate. The optimized CSAM settings were used for the characterization studies in the following sections. It should be noted that this process optimization study is valid for low-pressure cold spray process within the design space defined by Eqs. (1)–(3), as applied in this work for regolith deposition.

3.3. Effect of number of spray pass on coating thickness

The PTFE samples were cold sprayed with varying numbers of passes (i.e., 3, 5, and 7 passes). As shown in Fig. 7a, the coating thickness (mean) consistently increased up to 7 spray passes, rising from $\sim 14 \pm 2$ μm to 19 ± 4 μm. This trend can be attributed to the kinetic impact of the incoming regolith particles, which induces

a shot-peening-like tamping effect [61]. This behavior can be seen in the cross-sectional SEM images in Fig. 7b, which compares the microstructure of 3-pass, 5-pass, and 7-pass, along with the EDX map of the 7-pass specimen, confirming successful regolith deposition.

However, it should be noted that while increasing the number of spray passes resulted in relatively thicker coatings, the incremental gains became negligible at higher pass numbers. This suggests that with higher number of passes, the ability of incoming particles to embed decreases, and further deposition may result in particle rebound or surface erosion (see Fig. 1d). This balance between compaction-driven densification and erosion-induced material loss explains both the initial coating growth and the eventual diminishing returns at higher spray passes [62]. These findings indicate that the number of spray passes should be carefully optimized, as additional deposition may compromise coating uniformity.

3.4. Mechanical tests

The tensile tests were conducted using the rectangular specimens (see Fig. 7c) with dimensions of 127 mm (length) \times 12.7 mm (width) \times 3.2 mm (thickness), and a gauge length of 50 mm. Fig. 7d shows the load-displacement curves of the specimens subjected to varying numbers of spray passes. The yield strength remained relatively consistent across all samples, indicating that regolith deposition did not compromise the elastic properties of the PTFE. On the other hand, the coated specimens exhibited reduced ductility comparing to the pristine (non-coated) PTFE. This reduction in ductility is likely due to the incorporation of the brittle regolith phase into the PTFE matrix that might hinder polymer chain mobility, thereby limiting the material's ability to deform. However, ductility remained largely consistent for the 5- and 7-pass specimens, showing no notable variation with increasing spray passes, but was comparatively lower for the 1-pass specimen.

Fig. 7e presents the distribution of yield strength and ultimate tensile strength (UTS) for the specimens. While the yield strength remained relatively unchanged, increasing the number of spray passes led to a reduction in UTS, with a 10.5% decrease observed for the 1-pass specimen and 15% for the 5- and 7-pass specimens, compared to the pristine (baseline) PTFE. However, no significant difference in UTS was observed among all the coated specimens. This indicates that beyond the first spray pass, additional layers may not substantially affect the UTS, likely due to coating saturation on load transfer. This finding further highlights the need for a more comprehensive DoE that explicitly considers the effect of the number of spray passes under varying CSAM process parameters. Collectively, the results suggest that the initial application (i.e., first layer deposition) of the regolith coating has the most pronounced impact on mechanical performance, affecting both ductility and strength. Therefore, the inclusion of the regolith phase via CSAM should be carefully considered, as it may reduce the material's load-bearing capacity.

3.5. Hardness tests

The hardness of the fabricated coatings was evaluated via nanoindentation, using a controlled force applied through a Berkovich indenter [63] to penetrate the regolith coating surface. The indentation

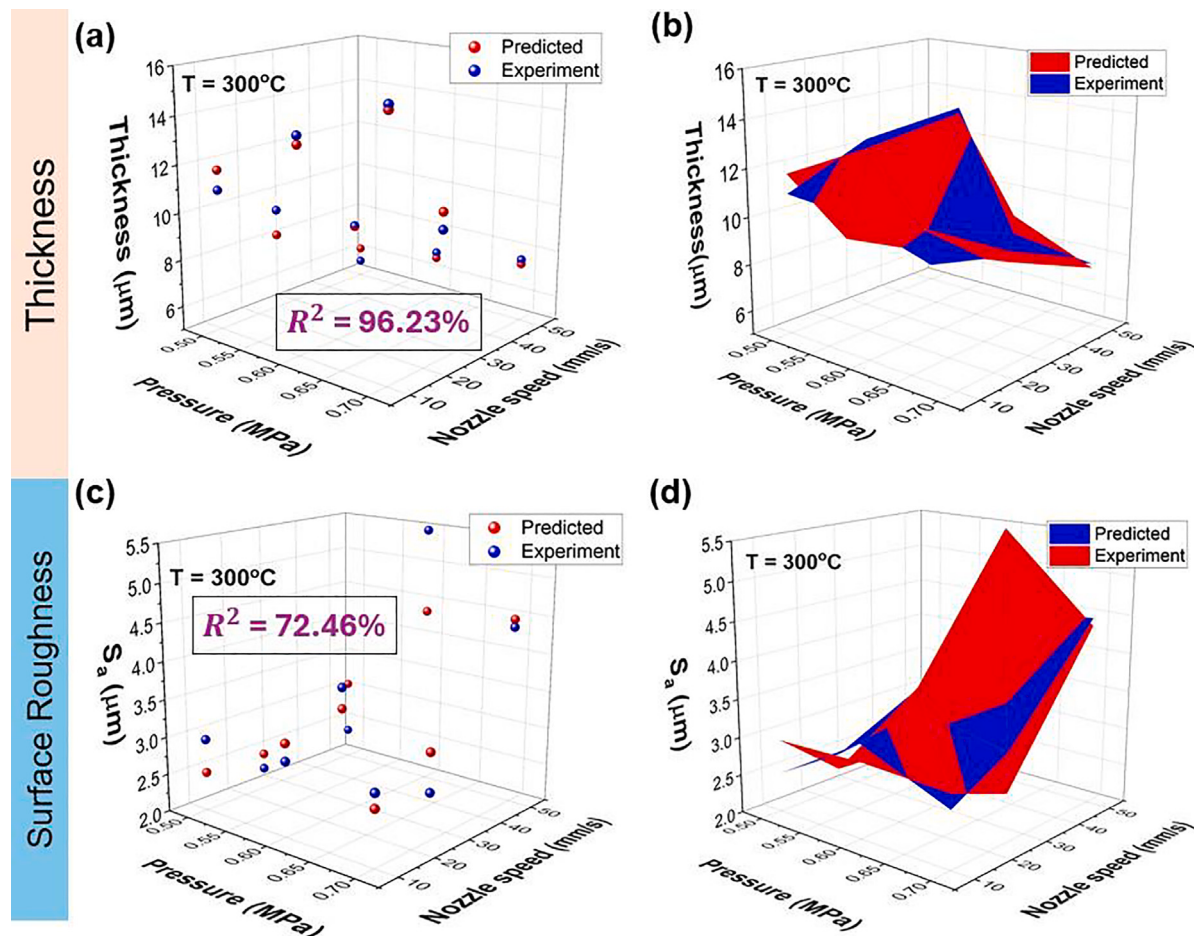


Fig. 5. Comparison between predicted and experimental values of (a-b) coating thickness and (c-d) surface roughness.

Table 4
ANOVA response table for the surface roughness.

Source	DF	Adj SS	Adj MS	F-Value	P-Value
Pressure (MPa)	2	2.6187	1.3094	2.38	0.209
Temperature (°C)	1	1.3668	1.3668	2.48	0.190
Nozzle speed (mm/s)	2	0.4585	0.2293	0.42	0.685
Pressure (MPa) × Temperature (°C)	2	1.1791	0.5896	1.07	0.424
Pressure (MPa) × Nozzle speed (mm/s)	4	2.4522	0.6131	1.11	0.460
Temperature (°C) × Nozzle speed (mm/s)	2	2.9059	1.4529	2.64	0.186
Error	4	2.2028	0.5507		
Total	17	13.1841			

data were analyzed using the Oliver–Pharr method [64], based on the principles of elastic contact theory. The key parameters in indentation testing are: P_m = maximum load, h_m = maximum indentation depth, h_f = residual indentation depth, and $S = dP/dh$ refers to the elastic contact stiffness (the slope of the unloading curve at the initial stage). Using these measured parameters, along with the following equations [64], the hardness and elastic modulus of the tested materials can be determined.

$$H_m = \frac{P_m}{A} \quad (4)$$

$$E_r = \frac{\sqrt{\pi}S}{2\beta\sqrt{A}} \quad (5)$$

$$\frac{1}{E_m} = \frac{1 - \nu^2}{E} + \frac{1 - \nu_i^2}{E_i} \quad (6)$$

where, A = contact area, E_r = indentation modulus (reduced modulus), E = Young's modulus of indenter, ν = Poisson's ratio of indenter, E_i =

elastic modulus of the tested sample, ν_i = Poisson's ratio of the tested sample, β = constant related to the indenter geometry.

Fig. 8a–b show the force-penetration depth curves and the corresponding hardness values for coatings produced with 1, 5, and 7 spray passes. Among the coated samples, the single-pass regolith coating exhibited the steepest slope and lowest penetration depth (Fig. 8a), indicating a higher resistance to indentation (i.e., greater hardness). This behavior can be attributed to denser particle packing and direct impact with the substrate at the initial spray pass (first layer), along with a reduced likelihood of defects (e.g., porosity) in the thinner coating (see Fig. 7a–b). The mechanical test results in Fig. 7d–e further corroborate this trend, where the single-pass coating achieved the highest yield strength and UTS among the specimens with multiple spray passes.

Conversely, as the number of spray passes increased, the penetration depth also rose (Fig. 8a), leading to a reduction in hardness (Fig. 8b). Unlike CSAM of metallic particles on metal substrates, where the tamping effect from successive particle impacts typically enhances

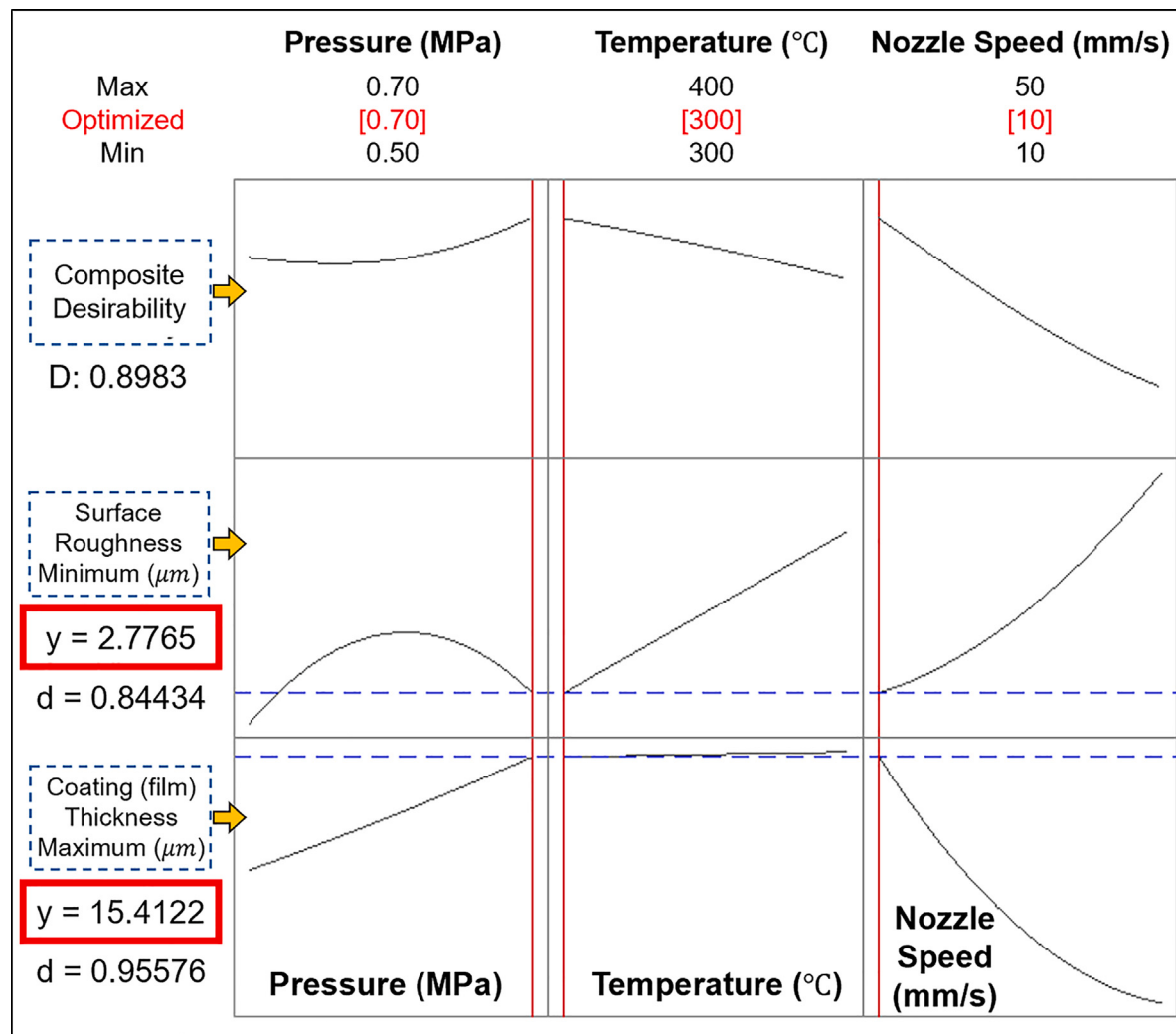


Fig. 6. Multi-objective optimization of surface roughness and coating thickness.

hardness of the underlying material [62], an opposite trend was observed for brittle regolith particles impacting polymer (PTFE) substrate. This difference likely arises from the lack of strain-hardening capability in polymers. Instead, impact of regolith particles may induce surface erosion and microcrack initiation, which collectively degrade hardness as seen in Fig. 8b. In this context, the deposition mechanism of regolith particles resembles the brittle fracture and erosion phenomena often observed during the co-deposition of metal–ceramic (cermet) systems in the CS process [65]. Beyond surface erosion, the buildup of thicker deposits also increases the likelihood of microcrack formation within the coating, which may further reduces load-bearing capacity (see Fig. 7e) and contributes to the observed decrease in hardness.

Notably, the regolith coating did not enhance hardness relative to baseline (pristine) PTFE; instead, the mean hardness decreased by 31.32% (1 pass), 43.58% (5 passes), and 51.78% (7 passes) compared with pristine PTFE. This reduction is likely attributable to (i) the as-sprayed surface roughness and local porosity, (ii) a discontinuous, particle-embedded layer rather than a continuous film formation, and (iii) substrate influence during indentation. These findings suggest that achieving a continuous regolith film may be required to avoid compromising the polymer's intrinsic hardness and to enable potential hardness enhancement.

3.6. Effect of spray pass number: Statistical analysis

A dedicated ANOVA was conducted to evaluate the statistical influence of number of spray pass on coating thickness, hardness, yield strength, and UTS. For each parameter, three respective measurements were included in the analysis. The ANOVA results for coating thickness and mechanical properties are presented in Table 5. The results indicate that the number of spray pass has a statistically significant effect on coating thickness and UTS ($p < 0.05$), with coating thickness being the most affected, followed by UTS. In contrast, hardness ($p = 0.120$) and yield strength ($p = 0.128$) are not significantly influenced by spray pass count, suggesting that these properties are governed primarily by localized microstructural features and substrate-dominated mechanical behavior rather than the total number of deposition layers. Overall, the ANOVA findings demonstrate that while increasing the number of spray passes significantly impacts coating thickness and tensile strength, it does not produce notable changes in coating hardness or yield strength.

3.7. Adhesion tests

To evaluate the interfacial adhesion between the regolith coating and the underlying polymer substrate, both qualitative and quantitative tests were conducted. First, the qualitative cross-cut adhesion tests were performed in accordance with the ASTM D3359 [53]. In this context, scratch tests were carried out on the single-pass surface

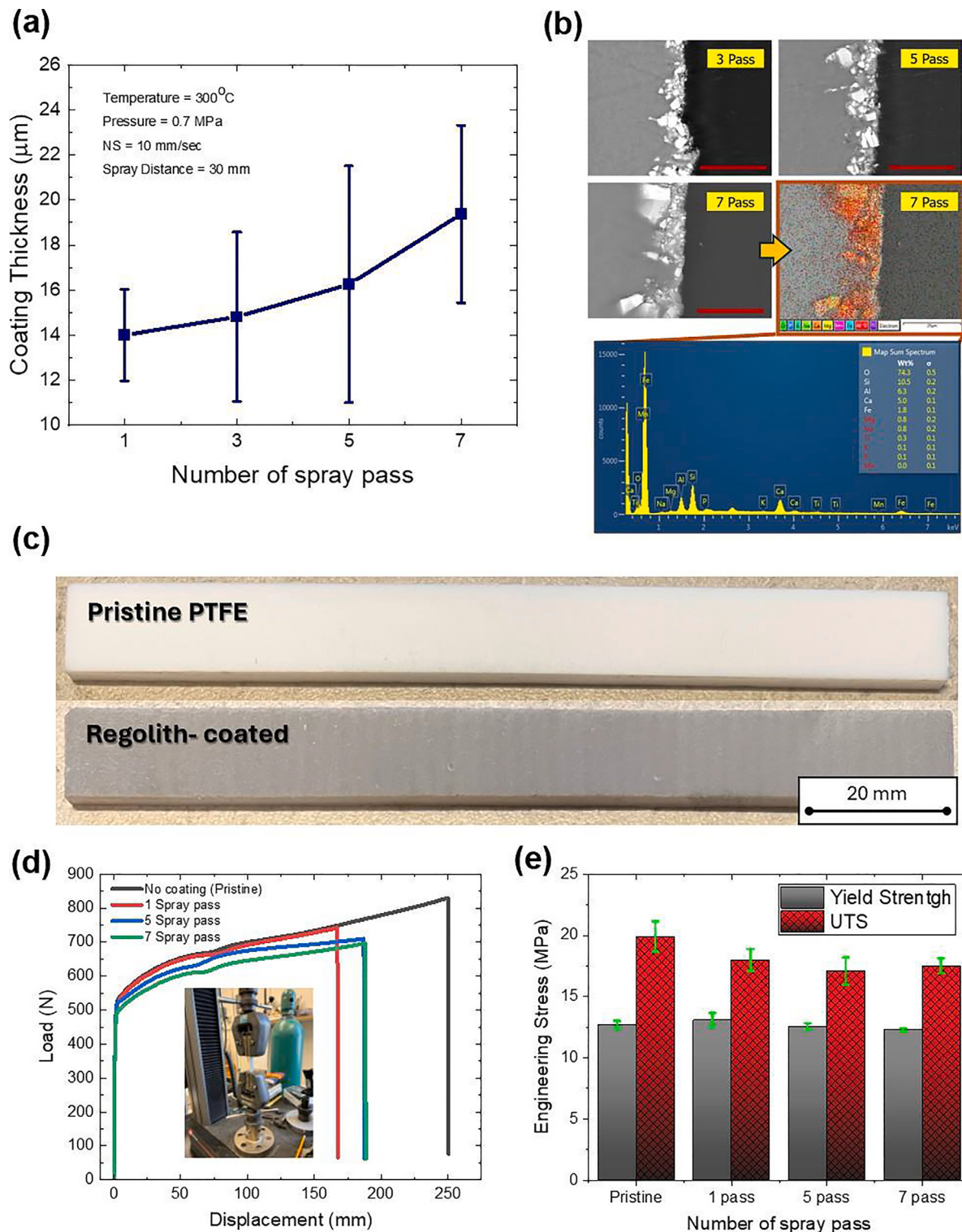


Fig. 7. Mechanical characterization of regolith-deposited specimens: (a) Variation of coating thickness with spray pass count; (b) Cross-sectional SEM images showing coating thickness for different numbers of spray passes; (c) Representative tensile-test specimen; (d) Load-displacement curves of the specimens; (e) Variation in yield strength and UTS across the specimens. (Scale bar in Fig. 7b = 30 μm).

following the ASTM D3359 standard for coatings thinner than 50 μm . Parallel scratches spaced 1 mm apart were made (Fig. 9a), and pressure-sensitive tape was applied and removed over the area. Visual inspection (Fig. 9b), along with magnified examination of both the tape and coating surfaces (Fig. 9c-d), revealed no noticeable peeling or detachment. According to the ASTM D3359 scale as shown in Fig. 9e [53], the coating scored 5B, demonstrating excellent adhesion.

In addition to qualitative evaluations, quantitative tensile pull-off adhesion tests were conducted following ASTM D4541 [53,66], owing to its greater suitability for polymeric substrates compared to the ASTM C633 standard. [67] To improve surface roughness and adhesive bonding, 14.2 mm diameter test dollies were sanded before being bonded to the regolith-coated specimens using an epoxy adhesive (3M 460), cured at room temperature for 24 h. A controlled tensile load was then

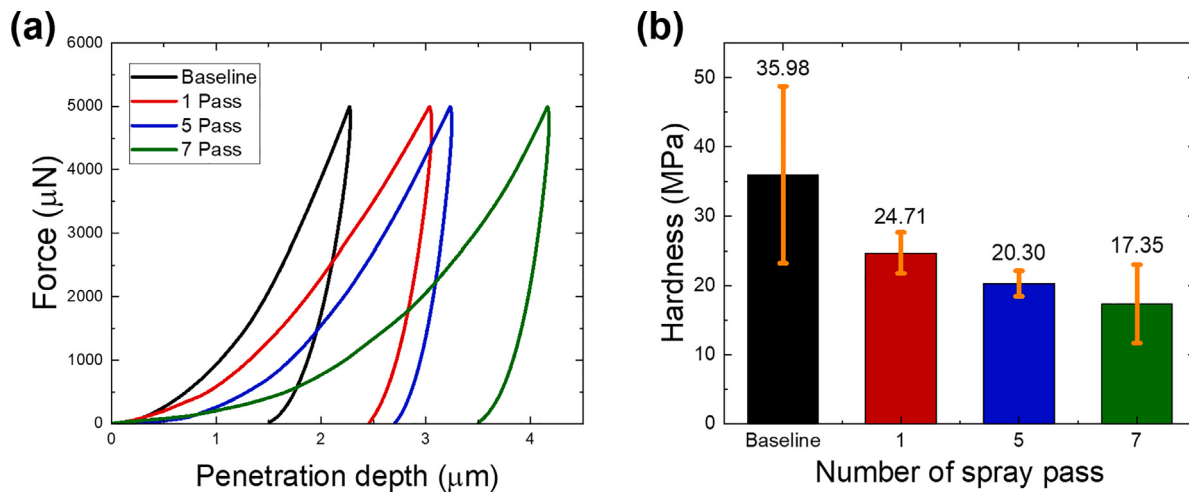


Fig. 8. (a) Force-penetration depth curves; (b) Variation of hardness with number of spray passes.

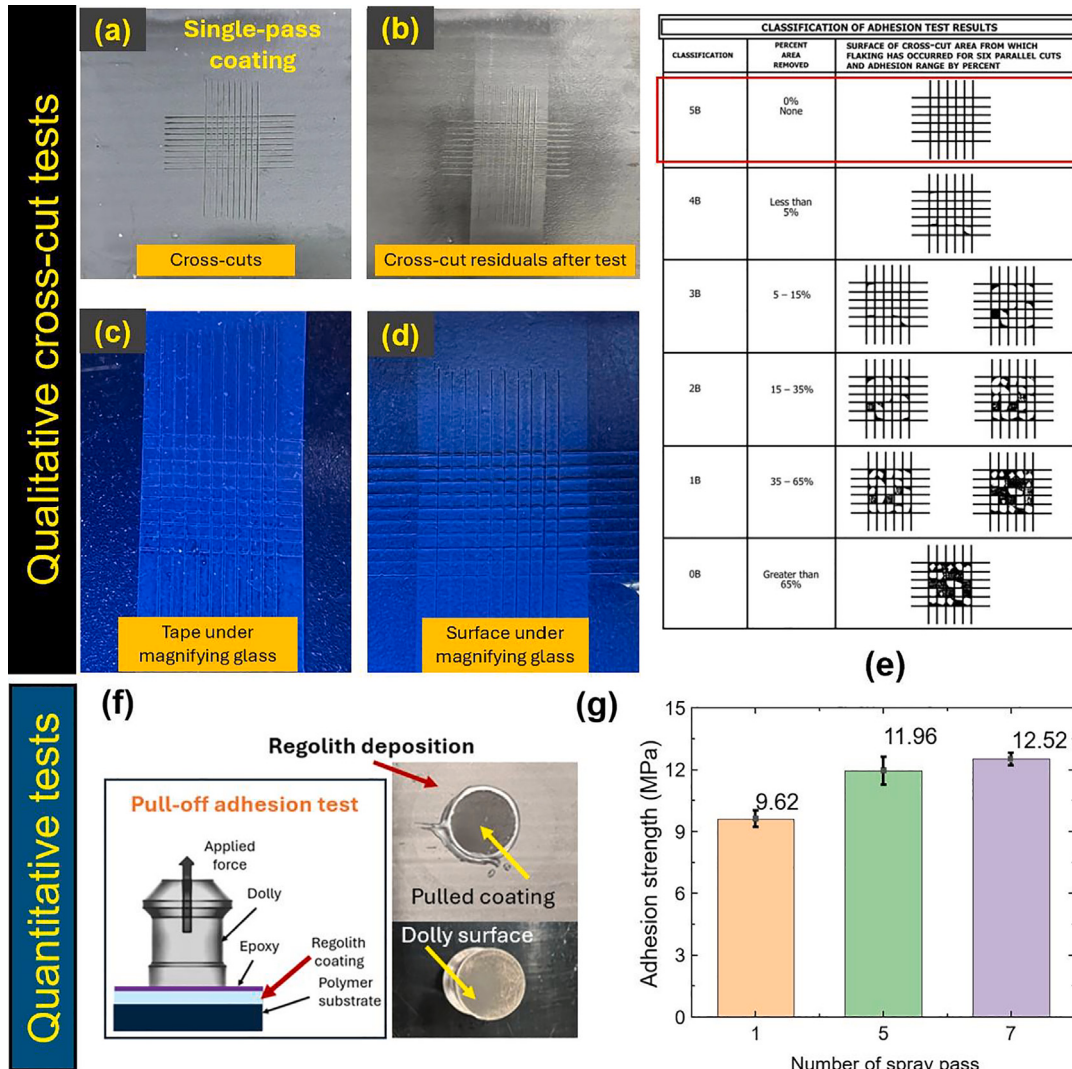


Fig. 9. Adhesion performance of the regolith deposited specimens: Coating surface (a) before and (b) after the scratch test; (c) removed tape and (d) coating surface under the magnifying glass following the test; (e) ASTM D3359 adhesion test scale; (f) Schematic of the pull-off adhesion test (left panel) and representative images of the pulled-off coating (right panel); (g) Adhesion strength of the resulting regolith coatings.

Table 5

ANOVA results for the effects of spray pass number on mechanical properties.

Parameter	Source	DF	Adj SS	Adj MS	F-Value	P-Value
Coating thickness	No. of spray pass	3	726.2	242.06	7.79	0.009
	Error	8	248.7	31.09		
	Total	11	974.9			
Hardness	No. of spray pass	3	572.5	190.83	2.66	0.120
	Error	8	574.9	71.86		
	Total	11	1147.4			
Yield strength	No. of spray pass	3	0.9908	0.3303	2.56	0.128
	Error	8	1.0311	0.1289		
	Total	11	2.0218			
UTS	No. of spray pass	3	14.009	4.6698	4.69	0.036
	Error	8	7.970	0.9962		
	Total	11	21.979			

applied at 2 MPa/s using a pull-off adhesion tester (*Elcometer 510*) (Fig. 9f). Since regolith particles are embedded in the PTFE substrate (Fig. 7b), strong bonding between the epoxy and regolith surface is critical to ensure cohesive rather than adhesive failure during testing. However, the inherently hydrophobic nature of the PTFE surface limited epoxy adhesion, resulting in partial coating detachment. As a result, most embedded particles remained on the substrate after testing. To address this issue, we employed a moderately hydrophobic substrate, Acrylonitrile Butadiene Styrene (ABS), which has a water contact angle of approximately $\sim 75^\circ$ – 90° [68]. The ABS substrate (*McMaster*) was coated using the optimized CSAM parameters identified in Section 3.2, with varying numbers of spray passes, followed by the pull-off adhesion tests.

Fig. 9g shows the trend in adhesion strength as a function of spray pass count. All regolith deposits exhibited strong adhesion strength exceeding 9 MPa. Notably, the adhesion strength increased with the number of spray passes, showing improvements of 24.32% with 5 passes and 30.15% with 7 passes compared to the single pass deposit. This trend can be attributed to the tamping effect from the repeated impacts of incoming regolith particles at higher spray pass counts, which in turn enhances adhesion strength [62]. Furthermore, the increased surface roughness and enlarged effective contact area associated with the relatively non-uniform coating morphology at higher spray passes (see Fig. 7a) may provide additional anchoring sites, thereby further improving adhesion strength. Overall, the cold-sprayed regolith coatings exhibited adhesion strengths comparable to those reported in previous studies on polymer metallization [41], highlighting the effectiveness of the process in establishing robust interfacial bonding. Furthermore, the results confirmed the feasibility of depositing regolith via CS on other polymer systems (e.g., ABS), thereby underscoring the potential of CS-based regolith coatings for a wide range of functional applications.

3.8. A case study on the thermal resistance of regolith coatings

To evaluate the thermal resistance of the fabricated regolith coatings, a case study was designed and implemented using the experimental setup shown in Fig. 10a. A programmable heat gun was positioned at a fixed distance of 3 mm above the PTFE specimen's surface (i.e., 50.8 mm (w) \times 50.8 mm (l) \times 3.2 mm (h)) and operated at an airflow temperature of \sim 200 °C to provide stable heating. The electrical power, nozzle diameter, and airflow rate of the heat gun were 1800 W, 20 mm, and 300 L/min, respectively. The specimen was coated with regolith using the optimized cold spray parameters (i.e., $T = 300$ °C, $P = 0.7$ MPa, and NS = 10 mm/s). A thin-film Type J thermocouple was attached to the center of the bottom surface of the sample, as shown in Fig. 10a (right panel). The bottom material was fiberboard with a thermal conductivity of \sim 0.065 W/mK [69]). The thermocouple was

interfaced with a data acquisition system for continuous temperature monitoring throughout the heating process, operating at a sampling frequency of 2000 Hz.

Fig. 10b presents the comparative temperature–time response of the baseline (pristine) and regolith-coated PTFE samples, where the bottom surface temperature was continuously monitored. In this controlled experiment, the samples were subjected to heating from room temperature until the bottom surface reached 150 °C. The results indicate that the regolith coating functions as such a thermal barrier, where it required 37.5% more time for the coated sample's bottom surface to reach 150 °C compared to the pristine sample (see Fig. 10b). In addition, at 160 s, when the baseline bottom surface reached 150 °C, the temperature of the regolith-coated sample remained 8.25% (i.e., \sim 137 °C) lower than that of the pristine PTFE. This improvement can be attributed to the intrinsic thermophysical properties of the oxide constituents within the regolith. These oxides possess high melting points and low thermal conductivities, which absorb and dissipate incident heat more effectively than the pristine polymer, functioning as a thermal barrier. Collectively, the results reveal that regolith-based coatings can enhance the thermal resistance of the polymeric substrates by reducing heat transfer through the material thickness, thereby highlighting their promise as thermal protection coatings.

4. Lunar considerations for CSAM

As conceptually depicted in Fig. 11, the solid-state nature of the CSAM can offer unique advantages in lunar conditions over the phase-change-based AM techniques (e.g., powder bed fusion, directed energy deposition, fused filament fabrication). These advantages include: (i) direct use of regolith as feedstock without complex melting process; (ii) reduced thermal effects due to the absence of high-temperature phase changes; and (iii) lower residual stresses. Under the ultra-high vacuum conditions of the Moon (i.e., \sim 10⁻¹² torr (night) to \sim 10⁻¹⁰ torr (day) [70]), feedstock materials used in phase-change and ink-based AM techniques tend to rapidly evaporate or vaporize [3]. Consequently, these methods require operation within pressurized environments, which may limit their suitability for critical on-site repair and manufacturing missions within the Moon's inherent habitat. These limitations are further intensified during lunar daytime, when the Moon's surface temperature can exceed 120 °C [71]. Moreover, phase-change AM methods might be highly susceptible to the effects of lunar microgravity, which can lead unstable melt pools and unpredictable solidification, eventually compromising the quality of fabricated components. As such, the combination of intense heat, near-zero atmospheric pressure, and microgravity can pose significant challenges for phase-change and ink-based AM techniques on the Moon.

Unlike phase-change-based AM methods, the Moon's inherent vacuum conditions may present promising advantages for the implementation of CSAM for ISRU. This is because the CSAM fundamentally relies on pressure differentials to accelerate functional feedstock powders (e.g., regolith) to the desired velocities for successful deposition. Even with a relatively modest compressed gas source, the pressure difference between the source and the surrounding vacuum can produce sufficiently high particle velocities for effective deposition. Furthermore, the absence of atmospheric drag can eliminate energy losses, allowing particles to maintain higher terminal velocities over longer travel distances. This can also help mitigate the formation of the bow-shock near the substrate, which is known to adversely affect particle deposition and bonding [72,73]. Prior studies on CSAM under vacuum conditions have confirmed the beneficial effects of reduced ambient pressure in suppressing bow-shock formation, thereby facilitating more efficient particle deposition. [74–76] Besides, CSAM is expected to be largely unaffected by the Moon's microgravity due to its high-velocity and directional particle flow. Taken together, these factors can

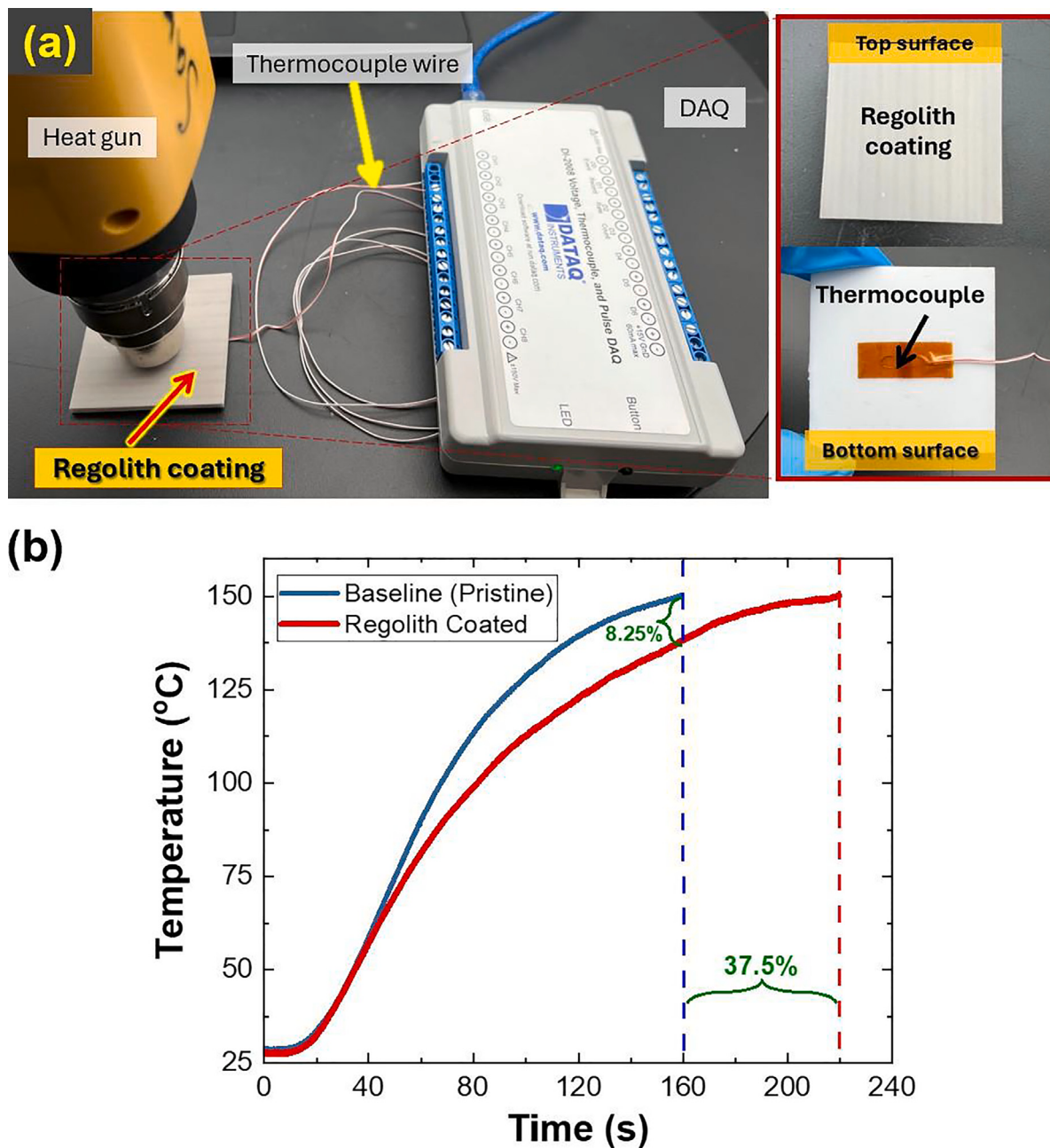


Fig. 10. Thermal resistance test: (a) Experimental setup; (b) Temperature variation over time.

position CSAM as a promising candidate for ISRU on the Moon, without requiring a dedicated pressurized environment.

Despite its advantages, CSAM might face several critical limitations in the lunar environment. A major challenge would be the suitability of lunar regolith as feedstock as its abrasive, angular, and brittle nature requires significant preprocessing to feedstock demands of CSAM. While the Moon's vacuum and low gravity offer benefits, they might also complicate particle control and substrate interaction. These technical challenges highlight the need for continued experimental and numerical research (e.g., two-phase rarefied flows) under vacuum conditions to capture the impact velocity evaluation and impact dynamics of irregular-shaped regolith particles. Such studies are essential to elucidate the underlying momentum transfer, particle deformation, and bonding mechanisms that govern deposition in low-pressure (vacuum) environments. Ultimately, advancing this understanding might enable a more comprehensive assessment of the feasibility and process optimization of CSAM for space manufacturing and ISRU applications.

5. Conclusion

In this study, CSAM using moon regolith simulant (LHS-1D) was investigated to elucidate the surface and interfacial interactions governing the formation of coatings on high-performance polymers such as PTFE. The primary objective was to assess the feasibility of CSAM for depositing well-adhered regolith coatings on polymeric substrates as a step toward ISRU on the Moon. Based on the results, the following conclusions can be drawn:

- Increasing the CSAM gas temperature and pressure enhances regolith coating thickness by facilitating deeper particle penetration into the polymer substrate, thereby yielding a thicker deposition.
- Regolith coating thickness increases with the number of spray passes, but the deposition becomes less uniform due to potential erosion from the incoming regolith particles.

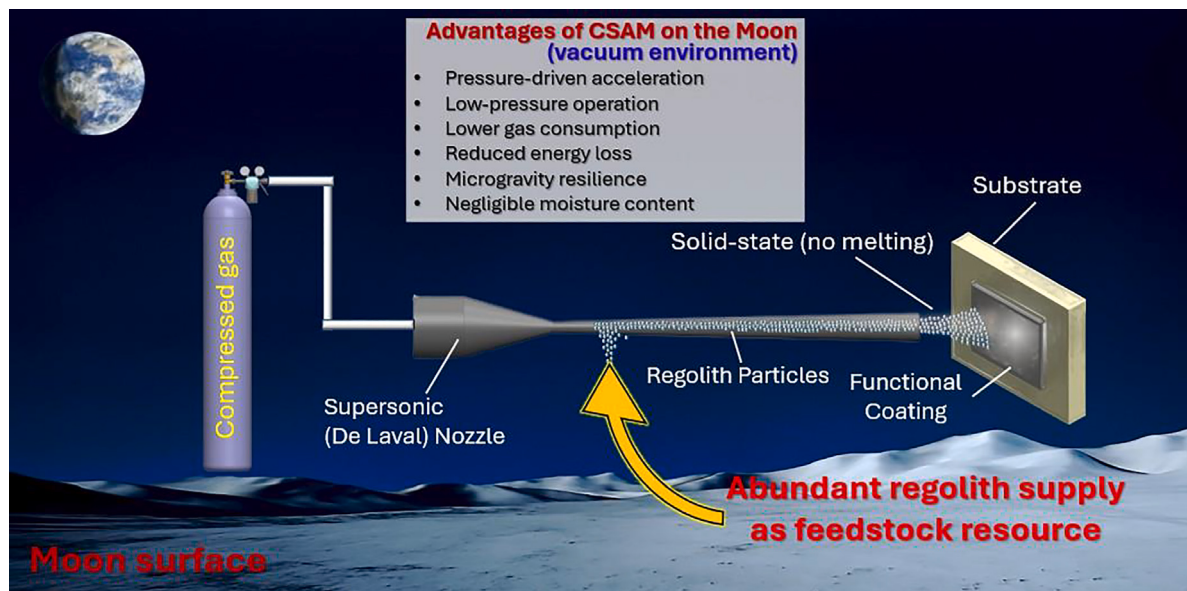


Fig. 11. Conceptual illustration of CSAM in the lunar environment.

- While the yield strength remained largely unchanged, UTS decreased by 10.5% after one spray pass and 15% for 5- and 7-pass specimens compared to pristine PTFE.
- Increasing the number of spray passes resulted in a reduction in coating hardness, with the decrease of 31.24% for 1-pass, 43.58% for 5-pass and 51.78% for 7-pass coatings, respectively, relative to the pristine PTFE.
- The regolith coatings achieved an adhesion rating of 5B, indicating excellent adhesion strength per ASTM D3359. In addition, all regolith deposits exhibited strong adhesion strengths exceeding 9 MPa.
- Although the regolith coating did not enhance the mechanical strength and hardness relative to pristine PTFE, it improved the thermal resistance (~8.25%) of the underlying polymer.

This study demonstrated the potential of CSAM to produce coatings from lunar regolith on polymeric substrates under terrestrial conditions. Nevertheless, the Moon's low gravity, lack of atmosphere, and extreme temperature fluctuations are expected to affect coating quality. Hence, future work should focus on testing CSAM under lunar-like conditions, as well as developing ISRU-based feedstock preparation strategies. In parallel, regolith deposition using high-pressure cold spray systems should be investigated, as such systems may enable the fabrication of thicker, denser, and mechanically robust coatings. Therefore, feasibility assessments should address these factors by simulating lunar conditions, optimizing CSAM process conditions, evaluating thermal cycling effects on coating integrity, and developing ISRU-based feedstock preparation strategies to support future lunar exploration missions.

CRediT authorship contribution statement

Sazedur Rahman: Writing – review & editing, Writing – original draft, Visualization, Methodology, Investigation, Formal analysis, Conceptualization. **Semih Akin:** Writing – review & editing, Writing – original draft, Validation, Supervision, Resources, Project administration, Methodology, Investigation, Formal analysis, Conceptualization.

Declaration of competing interest

The authors declare that they have no known competing financial interests or personal relationships that could have appeared to influence the work reported in this paper.

Acknowledgments

The authors acknowledge the internal funding support from the Department of Mechanical, Aerospace, and Nuclear Engineering (MANE) at Rensselaer Polytechnic Institute (RPI).

Data availability

Data will be made available on request.

References

- [1] Florian Neukart, Towards sustainable horizons: A comprehensive blueprint for Mars colonization, *Heliyon* 10 (4) (2024) e26180.
- [2] A.S. Krasilnikov, M.A. Ivanov, S.S. Krasilnikov, J.W. Head, Stratigraphic cross-sections, geologic history, and provenance of material at the candidate landing sites of the Artemis missions, *Icarus* 420 (2024) 116190.
- [3] Mohammad Azami, Zahra Kazemi, Sare Moazen, Martine Dubé, Marie-Josée Potvin, Krzysztof Skoneczny, A comprehensive review of lunar-based manufacturing and construction, *Prog. Aerosp. Sci.* 150 (2024) 101045.
- [4] Kevin W. Farries, Phillip Visintin, Scott T. Smith, Philip van Eyk, Sintered or melted regolith for lunar construction: state-of-the-art review and future research directions, *Constr. Build. Mater.* 296 (2021) 123627.
- [5] NASA Office of Inspector General, NASA's management of the artemis missions (IG-22-003), 2021, <https://oig.nasa.gov/office-of-inspector-general-oig/ig-22-003/>. (Accessed 20 October 2025).
- [6] Astro robotic Technology, Astro robotic selects united launch alliance vulcan centaur rocket to launch its first mission to the moon, 2019, (Accessed 20 October 2025).
- [7] SpaceX, Moon — Human spaceflight, 2025, <https://www.spacex.com/humanspaceflight/moon>. (Accessed 04 October 2025).
- [8] J.N. Rasera, J.J. Cilliers, J.A. Lamamy, K. Hadler, The beneficiation of lunar regolith for space resource utilisation: A review, *Planet. Space Sci.* 186 (2020) 104879.
- [9] Yushen Wang, Liang Hao, Yan Li, Qinglei Sun, Mingxi Sun, Yuhong Huang, Zheng Li, Danna Tang, Yijing Wang, Long Xiao, In-situ utilization of regolith resource and future exploration of additive manufacturing for lunar/martian habitats: A review, *Appl. Clay Sci.* 229 (2022) 106673.
- [10] Maxim Isachenkov, Svyatoslav Chugunov, Iskander Akhatov, Igor Shishkovsky, Regolith-based additive manufacturing for sustainable development of lunar infrastructure – An overview, *Acta Astronaut.* 180 (2021) 650–678.
- [11] Jared M. Long-Fox, Daniel T. Britt, Characterization of planetary regolith simulants for the research and development of space resource technologies, *Front. Space Technol.* 4 (2023) 1255535.
- [12] Exolith Lab, LHS-1D lunar highlands simulant specification sheet, 2023, https://cdn.shopify.com/s/files/1/0398/9268/0862/files/LHS-1D_SPEC_SHEET_DEC_2023.pdf?v=1745852728. (Accessed 30 May 2025).

- [13] Wucheng Sun, Fen Dang, Yan Zhou, Shifeng Wen, Cheng Zhou, Yusheng Shi, Lieyun Ding, Additive manufacturing of lunar regolith: A review, *Addit. Manuf. Front.* (2025) 200225.
- [14] Ayushi Gupta, Sonika Sahu, Piyush Ukey, Atish Kumar, Vivek Gupta, Anish Sachdeva, Narendra Kumar, Additive manufacturing for space applications: A review of processes, properties, and prospects, *Acta Astronaut.* (2025).
- [15] Miguel Hoffmann, Alaa Elwany, In-space additive manufacturing: A review, *J. Manuf. Sci. Eng.* 145 (2) (2023) 020801.
- [16] Caterina Iantaffi, Chu Lun Alex Leung, George Maddison, Eral Bele, Samy Hocine, Rob Snell, Alexander Rack, Martina Meisnar, Thomas Rohr, Iain Todd, Peter D. Lee, Laser additive manufacturing of lunar regolith simulant: New insights from *in situ* synchrotron X-ray imaging, *Addit. Manuf.* 101 (2025) 104711.
- [17] Vinay Kenny, Salil Bapat, Ajay P. Malshe, Exploring the feasibility of processing Inconel-718 and highland regolith composite using laser-assisted powder bed fusion, *Procedia CIRP* 121 (2024) 198–203.
- [18] Caterina Iantaffi, Chu Lun Alex Leung, Elena Ruckh, Samy Hocine, Alexander Rack, Peter D. Lee, Real-time synchrotron X-ray Imaging of laser additive manufactured lunar Regolith simulant, *Acta Astronaut.* 233 (2025) 218–222.
- [19] Hailong Liao, Junjie Zhu, Shijie Chang, Gang Xue, Jingxi Pang, Haihong Zhu, Lunar regolith - AISI100Mg composite fabricated by selective laser melting, *Vacuum* 187 (2021) 110122.
- [20] Leonardo Caprio, Ali Gökhān Demir, Barbara Previtali, Bianca Maria Colosimo, Determining the feasible conditions for processing lunar regolith simulant via laser powder bed fusion, *Addit. Manuf.* 32 (2020) 101029.
- [21] Vamsi Krishna Balla, Luke B Roberson, Gregory W O'Connor, Steven Trigwell, Susmita Bose, Amit Bandyopadhyay, First demonstration on direct laser fabrication of lunar regolith parts, *Rapid Prototyp. J.* 18 (6) (2012) 451–457.
- [22] Ludger Overmeyer, Marvin Raupert, Matthias Pusch, Tjorben Griemsmann, André Katterfeld, Christoph Lotz, Laser powder directed energy deposition and substrate-free single layer powder bed fusion under micro-and lunar gravity conditions, *CIRP Ann* (2025).
- [23] Pial Das, Emil Umerov, Nicholas Dyrstad-Cincotta, Md Touhidul Islam Rimon, Matthew Mazurkivich, Sara Rengifo, William Scott, Yachao Wang, Sougata Roy, Exploring the erosion resistance of Al6061 metal matrix composite fabricated via additive manufacturing for future lunar exploration, *Prog. Addit. Manuf.* (2025) 1–17.
- [24] Tongcai Wang, Guangshuai Gu, Rihan Zhang, Qianshun Cui, Gong Wang, Additive manufacturing of lunar regolith via resin-based binder and material extrusion method for high-performance *in-situ* manufacturing on the moon, *Addit. Manuf. Front.* (2025) 200233.
- [25] Md Habibor Rahman, Anna K. Hayes, Krishna Muralidharan, Douglas A. Loy, Mohammed Shafae, Additive manufacturing of hydrogel-based lunar regolith pastes: A pathway toward *in-situ* resource utilization and in-space manufacturing, *J. Manuf. Process.* 118 (2024) 269–282.
- [26] Zifan Geng, Zhiwen Wu, Xiangyu Wang, Lizhi Zhang, Wei She, Ming Jen Tan, A novel 3D printing scheme for lunar construction with extremely low binder utilization, *Addit. Manuf.* 99 (2025) 104657.
- [27] Miranda Fateri, Achim Frick, Constantin Schuler, Tim Schubert, Jochen Hoffmann, Jacobus van der Walt, Michael Salinas, 3D printing of flexible parts out of lunar regolith simulant, *Acta Astronaut.* 229 (2025) 779–786.
- [28] Mohammad Azami, Pierre-Lucas Aubin-Fournier, Krzysztof Skonieczny, Enhancing economical lunar-based manufacturing by incorporating lunar regolith into polyether-ether-ketone (PEEK): material development, additive manufacturing, and characterization, *Prog. Addit. Manuf.* (2025) 1–7.
- [29] Maxim Isachenkov, Antonio Mattia Grande, Marco Mariani, Nora Lecis, Riccardo Casati, Laura Silvestroni, Giuseppe Sala, Magnetic beneficiation-a novel approach to facilitate additive manufacturing of lunar regolith ceramics by vat photopolymerization, *Addit. Manuf.* (2025) 104863.
- [30] Adolor David Aiyeiki, Andrey Tikhonov, Svyatoslav Chugunov, Improved additive manufacturing of lunar regolith simulant via digital light processing for *in-situ* resource utilization on the moon, *Acta Astronaut.* 232 (2025) 640–653.
- [31] Chuang Xiao, Ke Zheng, Shenggui Chen, Nan Li, Xin Shang, Feihong Wang, Jiahua Liang, Sadaf Bashir Khan, Yafei Shen, Bingheng Lu, et al., Additive manufacturing of high solid content lunar regolith simulant paste based on vat photopolymerization and the effect of water addition on paste retention properties, *Addit. Manuf.* 71 (2023) 103607.
- [32] Philipp Nieke, Jaroslaw Kita, Marc Häming, Ralf Moos, Manufacturing dense thick films of lunar regolith simulant EAC-1 at room temperature, *Mater.* 12 (3) (2019) 487.
- [33] Abhijith Kunnenparambil Sukumaran, Cheng Zhang, Sara Rengifo, Michael Renfro, Gia Garino, William Scott, Matthew Mazurkivich, Annette Gray, Gabriel Demengehi, Ellen Rabenberg, et al., Tribological and radiation shielding response of novel titanium-boron nitride coatings for lunar structural components, *Surf. Coat. Technol.* 476 (2024) 130300.
- [34] Paul Fuierer, Robert Calvo, Gregory Strobel, Dense, nano-grained, multi-phase ceramic coatings by dry aerosol deposition of lunar regolith simulant, *Addit. Manuf.* 35 (2020) 101304.
- [35] Robert Calvo, Paul Fuierer, Mechanical integrity of ceramic coatings on Kapton made by a dry aerosol deposition of lunar mare simulant, *Int. J. Appl. Ceram. Technol.* 20 (1) (2023) 395–409.
- [36] Joris Kadok, Simon Bulou, Thomas Gaulain, Patrick Choquet, Lunar regolith for plasma spray coatings, *Surf. Coat. Technol.* 490 (2024) 131111.
- [37] Biliyar N. Bhat, Aerospace materials characteristics, in: *Aerospace Materials and Applications*, in: *Progress in Astronautics and Aeronautics*, American Institute of Aeronautics and Astronautics, Inc., 2018, pp. 11–208.
- [38] Ádám Kalácska, V Parmentier, Patrick De Baets, G Kalácska, Wear investigation of PTFE, PEEK and UHMWPE-based reciprocating shaft seal materials with lunar/Martian regolith simulants, *Wear* (2025) 205791.
- [39] Gábor Kalácska, György Barkó, Tamás Bálint, Róbert Keresztes, László Székely, Zoltán Károly, Tribological effects of martian regoliths on stainless steel with natural and composite lip seal and packing materials, *Lubr.* 13 (4) (2025) 136.
- [40] Mohankumar Ashokkumar, Duraisamy Thirumalaikumarasamy, Tushar Sonar, Sampathkumar Deepak, Packirisamy Vignesh, Mani Anbarasu, An overview of cold spray coating in additive manufacturing, component repairing and other engineering applications, *J. Mech. Behav. Mater.* 31 (1) (2022) 514–534.
- [41] Ruslan Melentiev, Nan Yu, Gilles Lubineau, Polymer metallization via cold spray additive manufacturing: A review of process control, coating qualities, and prospective applications, *Addit. Manuf.* 48 (2021) 102459.
- [42] Jung-Ting Tsai, Semih Akin, Fengfeng Zhou, David F Bahr, Martin Byung-Guk Jun, Establishing a cold spray particle deposition window on polymer substrate, *J. Therm. Spray Technol.* 30 (4) (2021) 1069–1080.
- [43] Chieloka Ibekwe, Xuanjie Wang, Brandon Nicholas Bolzani, Connor O'Brien, Cooper James Waataja, Colin P Mahony, Jeffrey R Feller, Adam M Swanger, Jason W Hartwig, Shankar Narayan, Synthesis, optical performance characterization, and durability of electrosprayed PTFE-PEO materials for space applications, *ACS Appl. Mater. Interfaces* 16 (25) (2024) 32587–32598.
- [44] Martin Drábik, Oleksandr Polonskyi, Ondřej Kylian, Juraj Čechvala, Anna Artemenko, Ivan Gordeev, Andrei Choukourov, Danka Slavinská, Iva Matolínová, Hynek Biederman, Super-hydrophobic coatings prepared by RF magnetron sputtering of PTFE, *Plasma Process. Polym.* 7 (7) (2010) 544–551.
- [45] Jared M Long-Fox, Zoe A Landsman, Parks B Easter, Catherine A Millwater, Daniel T Britt, Geomechanical properties of lunar regolith simulants LHS-1 and LMS-1, *Adv. Space Res.* 71 (12) (2023) 5400–5412.
- [46] Yongjin Wang, Shengkai Wang, Qingzhao Chu, Dongping Chen, Pyrolysis kinetics of polytetrafluoroethylene (PTFE), *Int. J. Quantum Chem.* 125 (3) (2025) e70015.
- [47] Bruno Améduri, Hisao Hori, Recycling and the end of life assessment of fluoropolymers: recent developments, challenges and future trends, *Chem. Soc. Rev.* 52 (13) (2023) 4208–4247.
- [48] Hetal Parmar, Felice Rubino, Fausto Tucci, Giovanna Rotella, Pedro Poza, Pierpaolo Carbone, Manufacturing and cold spraying of hybrid composites—A path for metallizing thermoset matrix composites, *Surf. Coat. Technol.* 489 (2024) 131144.
- [49] Asghar Heydar Astaraee, Chiara Colombo, Sara Bagherifard, Insights on metallic particle bonding to thermoplastic polymeric substrates during cold spray, *Sci. Rep.* 12 (1) (2022) 18123.
- [50] Ahmed Fardan, Christopher C. Berndt, Rehan Ahmed, Numerical modelling of particle impact and residual stresses in cold sprayed coatings: A review, *Surf. Coat. Technol.* 409 (2021) 126835.
- [51] Roberta Falco, Sara Bagherifard, Cold spray additive manufacturing: A review of shape control challenges and solutions, *J. Therm. Spray Technol.* (2025) 1–19.
- [52] Rizaldy Hakim Ash Shiddiqy, Alief Wikarta, Agus Sigit Pramono, Jung Ting Tsai, et al., Addressing challenges in deposition efficiency and material compatibility in low-pressure cold spray systems, *Results Eng.* 26 (2025) 105065.
- [53] ASTM International, Standard test methods for rating adhesion by tape test, 2023, (Accessed 30 June 2025).
- [54] ASTM International, ASTM D4541-22: Standard Test Method for Pull-Off Strength of Coatings Using Portable Adhesion Testers, ASTM International, West Conshohocken, PA, 2022, <https://store.astm.org/d4541-22.html>.
- [55] Mathanbabu Mariappan, D Thirumalaikumarasamy, Ashokkumar Mohankumar, M Tamilselvi, Somasundara Kumar Balam, Effect of reflectivity and porosity analysis of plasma sprayed lanthanum zirconate/yttria stabilized zirconia based thermal barrier coating: design of experimental approach, *Int. J. Interact. Des. Manuf. (IJIDeM)* (2025) 1–15.
- [56] Luis Alonso, M.A. Garrido-Maneiro, Pedro Poza, A study of the parameters affecting the particle velocity in cold-spray: Theoretical results and comparison with experimental data, *Addit. Manuf.* 67 (2023) 103479.
- [57] A. Nastic, B. Jodoin, D. Poirier, J.-G. Legoux, Particle temperature effect in cold spray: a study of soft particle deposition on hard substrate, *Surf. Coat. Technol.* 406 (2021) 126735.
- [58] Semih Akin, Seungjun Lee, Seunghwan Jo, Duygu Gazioglu Ruzgar, Karthick Subramaniam, Jung-Ting Tsai, Martin Byung-Guk Jun, Cold spray-based rapid and scalable production of printed flexible electronics, *Addit. Manuf.* 60 (2022) 103244.
- [59] Moses A. Adaan-Nyiak, Ahmed A. Tiamiyu, Recent advances on bonding mechanism in cold spray process: A review of single-particle impact methods, *J. Mater. Res.* 38 (1) (2023) 69–95.
- [60] Ashokkumar Mohankumar, Thirumalaikumarasamy Duraisamy, Vignesh Packirisamy, Optimizing cold spray process parameters for AA2024/Al2O3 coatings to minimize wear loss via response surface methodology and particle swarm optimization, *J. Adhes. Sci. Technol.* (2025) 1–24.

- [61] Wojciech Okuniewski, Mariusz Walczak, Mirosław Szala, Effects of shot peening and electropolishing treatment on the properties of additively and conventionally manufactured Ti6Al4V alloy: A review, *Mater.* 17 (4) (2024) 934.
- [62] Xinying Wei, Hongxia Zhou, Shengyi Cong, Shuo Yin, Rocco Lupoi, The influence of subsequent impacts on underlying particles during cold spraying, *J. Mater. Res. Technol.* (2025).
- [63] V. Renuka, S. Venkateswara Rao, Tezeswi Tadepalli, Nanoindentation technique in characterizing cementitious materials—A review, *Mater. Today: Proc.* (2023).
- [64] Warren C. Oliver, George M. Pharr, Nanoindentation in materials research: Past, present, and future, *Mrs Bull.* 35 (11) (2010) 897–907.
- [65] Subin Antony Jose, Ashish K. Kasar, Pradeep L. Menezes, Cold spray deposition of cermets: insights into bonding mechanism and critical parameters, *Int. J. Adv. Manuf. Technol.* 133 (1) (2024) 1–23.
- [66] J. Lee, S. Akin, JR. Walsh, MBG Jun, H. Lee, YC Shin, A Nitinol structure with functionally gradient pure titanium layers and hydroxyapatite over-coating for orthopedic implant applications, *Prog. Addit. Manuf.* 9 (4) (2024) 1025–1038.
- [67] Ashokkumar Mohankumar, Duraisamy Thirumalaikumarasamy, Tushar Sonar, Mikhail Ivanov, Packkirisamy Vignesh, Rajangam Pavendhan, Mathanbabu Mariappan, Jinyang Xu, Cold spray processing of AA2024/Al2O3 coating on magnesium AZ31B alloy: Process parameters optimization, microstructure and adhesive strength performance of coating, *Int. J. Lightweight Mater. Manuf.* 7 (5) (2024) 721–737.
- [68] Vedrana Lovinčić Milovanović, Cédric Guyon, Ivana Grčić, Michael Tatoulian, Domagoj Vrsaljko, Modification of surface hydrophobicity of PLA/PE and ABS/PE polymer blends by ICP etching and CFx coating, *Mater.* 13 (23) (2020) 5578.
- [69] Mariana Palumbo, AM Lacasta, MP Giraldo, Laia Haurie, E Correal, Bio-based insulation materials and their hydrothermal performance in a building envelope system (ETICS), *Energy Build.* 174 (2018) 147–155.
- [70] Francis S. Johnson, James M. Carroll, Dallas E. Evans, Vacuum measurements on the lunar surface, *J. Vac. Sci. Technol.* 9 (1) (1972) 450–456.
- [71] National Aeronautics and Space Administration (NASA), Weather on the Moon, 2025, <https://science.nasa.gov/moon/weather-on-the-moon/>. (Accessed 31 July 2025), page last updated June 25, 2025.
- [72] J. Pattison, S. Celotto, A. Khan, W. O'neill, Standoff distance and bow shock phenomena in the Cold Spray process, *Surf. Coat. Technol.* 202 (8) (2008) 1443–1454.
- [73] Semih Akin, Puyuan Wu, Jung-Ting Tsai, Chandra Nath, Jun Chen, Martin Byung-Guk Jun, A study on droplets dispersion and deposition characteristics under supersonic spray flow for nanomaterial coating applications, *Surf. Coat. Technol.* 426 (2021) 127788.
- [74] Stephen G. Bierschenk, Desiderio Kovar, A nozzle design for mitigating particle slowing in the bow shock region during micro-cold spray of 8 YSZ films, *J. Aerosol Sci.* 179 (2024) 106360.
- [75] Stephen G. Bierschenk, Michael F. Becker, Desiderio Kovar, Gas and ceramic particle velocities for micro-cold spray, *J. Aerosol Sci.* 169 (2023) 106113.
- [76] Stephen G. Bierschenk, Desiderio Kovar, Micro-cold spray deposition of YSZ films from ultrafine powders using a pressure relief channel nozzle, *J. Therm. Spray Technol.* 33 (6) (2024) 2022–2033.